

## EXPLORING THE DIVERSITY OF GROUPS AT $0.1 < z < 0.8$ WITH X-RAY AND OPTICALLY SELECTED SAMPLES

J. L. CONNELLY<sup>1</sup>, DAVID J. WILMAN<sup>2</sup>, ALEXIS FINOGUENOV<sup>2,3</sup>, ANNIE HOU<sup>4</sup>, JOHN S. MULCHAEY<sup>5</sup>, SEAN L. MCGEE<sup>6,7</sup>,  
MICHAEL L. BALOGH<sup>6</sup>, LAURA C. PARKER<sup>4</sup>, ROBERTO SAGLIA<sup>2</sup>, ROBERT D. E. HENDERSON<sup>4,6</sup>, AND RICHARD G. BOWER<sup>7</sup>

<sup>1</sup> Max-Planck-Institut für Extraterrestrische Physik, Giessenbachstrasse, D-85748 Garching, Germany

<sup>2</sup> Max Planck Institute for Extraterrestrial Physics, P.O. Box 1312, Giessenbachstr., D-85741 Garching, Germany

<sup>3</sup> CSST, University of Maryland, Baltimore County, 1000 Hilltop Circle, Baltimore, MD 21250, USA

<sup>4</sup> Department of Physics & Astronomy, McMaster University, Hamilton ON L8S4M1, Canada

<sup>5</sup> Observatories of the Carnegie Institution, 813 Santa Barbara Street, Pasadena, CA 91101, USA

<sup>6</sup> Department of Physics and Astronomy, University of Waterloo, Waterloo, Ontario N2L 3G1, Canada

<sup>7</sup> Department of Physics, University of Durham, Durham DH1 3LE, UK

Received 2011 December 12; accepted 2012 July 4; published 2012 August 23

### ABSTRACT

We present the global group properties of two samples of galaxy groups containing 39 high-quality X-ray-selected systems and 38 optically (spectroscopically) selected systems in coincident spatial regions at  $0.12 < z < 0.79$ . The total mass range of the combined sample is  $\sim(10^{12}\text{--}5) \times 10^{14} M_{\odot}$ . Only nine optical systems are associable with X-ray systems. We discuss the confusion inherent in the matching of both galaxies to extended X-ray emission and of X-ray emission to already identified optical systems. Extensive spectroscopy has been obtained and the resultant redshift catalog and group membership are provided here. X-ray, dynamical, and total stellar masses of the groups are also derived and presented. We explore the effects of utilizing different centers and applying three different kinds of radial cut to our systems: a constant cut of 1 Mpc and two  $r_{200}$  cuts, one based on the velocity dispersion of the system and the other on the X-ray emission. We find that an X-ray-based  $r_{200}$  results in less scatter in scaling relations and less dynamical complexity as evidenced by results of the Anderson–Darling and Dressler–Schectman tests, indicating that this radius tends to isolate the virialized part of the system. The constant and velocity dispersion based cuts can overestimate membership and can work to inflate velocity dispersion and dynamical and stellar mass. We find  $L_X\text{--}\sigma$  and  $M_{\text{stellar}}\text{--}L_X$  scaling relations for X-ray and optically selected systems are not dissimilar. The mean fraction of mass found in stars, excluding intracluster light, for our systems is  $\sim 0.014$  with a logarithmic standard deviation of 0.398 dex. We also define and investigate a sample of groups which are X-ray underluminous given the total group stellar mass. For these systems the fraction of stellar mass contributed by the most massive galaxy is typically lower than that found for the total population of groups implying that there may be less intragroup medium contributed from the most massive member in these systems. Eighty percent of 15 underluminous groups have less than 40% of their stellar mass in the most massive galaxy which happens in less than 1% of cases with samples matched in stellar mass, taken from the combined group catalog.

*Key words:* galaxies: groups: general – X-rays: galaxies: clusters

*Online-only material:* color figures, machine-readable table

### 1. INTRODUCTION

The majority of galaxies in the universe lie in galaxy groups (Eke et al. 2004). Over cosmic time, groups grow hierarchically by accreting individual galaxies and smaller groups from their surrounding filamentary structure; thus, they are evolving environments. Even within limited redshift regimes, groups are observed to have diverse properties. Local studies (e.g., Zabludoff & Mulchaey 2000) reveal that their galaxy populations vary from being dominated by early-type (as in typical clusters) to late-type (as in the field population) galaxies. They range from “poor” groups containing a relatively small number of galaxies (commonly identified via optical selection methods) to massive systems (commonly identified via X-ray emission and weak lensing). The typical velocity dispersion within galaxy groups is comparable to the internal velocities of the galaxies they contain, making them ideal for galaxy–galaxy mergers and interactions. Therefore, groups are both important in their own right and as the predominant environment of galaxies.

Galaxy groups are not trivial to identify. At higher redshifts, they are most easily found via the X-ray emission of their intragroup medium (IGM). X-ray surveys are biased toward

selecting groups with rich IGM, and may not be typical of the dominant group population which shapes most galaxies in the universe. Samples selected optically may be dominated by overdensities of galaxies not yet fully virialized. Different physical processes are likely to be active in these two regimes and thus a comparison of groups selected via these two disparate methods can illuminate these physical phenomena.

To fully understand groups as the environment in which the majority of galaxies reside and evolve requires both a significant number of groups and significant information on the galaxy group members themselves. Wide-field surveys such as zCOSMOS and DEEP2 have identified many galaxy groups up to redshift  $\sim 1$  and  $\sim 1.3$ , respectively (Lilly et al. 2009; Gerke et al. 2007). The large sample sizes which these types of surveys yield allow for the rigorous determination of global trends in group properties. Evolution of low-mass galaxies appears to be accelerated in groups (Iovino et al. 2010) and transformation rates such as those from late- to early-type galaxy morphologies and from active to passive star formation activity are more than twice that in the field (Kovač et al. 2010). The buildup of stellar mass on the red sequence since  $z \sim 1$  involves  $L^*$  galaxies moving to the red sequence preferentially in groups (Cooper

et al. 2007). The low sampling rate and bright magnitude limits of these surveys mean, however, that the majority of groups have only a few confirmed members and thus that individual systems can be difficult to examine in detail.

A complementary approach to these large-volume surveys involves studying a smaller but well-defined and well-sampled selection of groups. The Group Environment Evolution Collaboration (GEEC) has taken this approach, defining samples at  $z \sim 0.5$  and recently extending studies up to a redshift of 1. Intermediate-redshift work has focused on optically selected groups and examined stellar masses, colors, morphologies, and star formation histories in these systems comparing to trends observed in the field (Wilman et al. 2005a, 2005b, 2008, 2009; Balogh et al. 2007, 2009; McGee et al. 2008, 2011). Our higher redshift study involves X-ray-selected systems and first results show a prominent transient population, migrating from the blue cloud to the red sequence, in these groups (Balogh et al. 2011b).

Comparing properties such as mass, X-ray luminosity and temperature, velocity dispersion, and richness via scaling relations allows us to explore the integrated properties of groups and clusters and how they relate to one another. In clusters, minimizing the scatter in these relations is a necessity in order to obtain accurate constraints on cosmological parameters. Through large, uniform samples, these relations are now relatively well constrained and seem to be very tight, even up to relatively high redshifts. Although group samples of similar size and quality are only recently available, group scaling relations exhibit a much greater scatter due to both larger measurement errors and greater intrinsic scatter in group properties (e.g., Osmond & Ponman 2004; Rykoff et al. 2008; Giodini et al. 2009; Balogh et al. 2011a). Understanding the scatter in the relations in the group regime is a key part of illuminating the physical processes at play.

In order to study groups spanning a significant mass and evolutionary range and to compare the results obtained from two of the most common group identification methods, we have defined two different samples within the same physical area, one via optical spectroscopy and the other via X-ray emission. In Finoguenov et al. 2009 (hereafter Paper I), we presented the X-ray observations of our fields and preliminary results for our sample of X-ray-selected groups. We have since finished an extensive spectroscopic campaign, significantly improving the sampling rate and depth of galaxies in our fields, and present here our full sample of X-ray and optically selected systems. In addition to X-ray-derived luminosities and masses, well-constrained membership now allows us to measure velocity dispersions and dynamical masses, stellar masses, and to search for dynamical complexity in our groups. In this paper, we present our catalog of groups and explore these global group properties. Future work will examine the galaxy populations of these groups and search for correlations with global properties.

In Section 2 we describe our samples. Section 3 describes the X-ray measurements of both optical- and X-ray-selected groups and Section 4 details the follow-up spectroscopy of the X-ray-selected systems. NIR measurements and galaxy stellar masses are described in Section 5. Global group properties including radial cuts, membership, and velocity dispersions are detailed in Section 6. X-ray and dynamical estimates of total group mass, and the total mass in stars are presented in Section 7. Dynamical complexity is explored in our systems in Section 8 via the Dressler–Schectman (DS) and Anderson–Darling (AD) tests. Section 9 presents the  $L_X$ – $\sigma$  relations for our samples. The “total” group masses are compared in Section 10. We discuss

the stellar and baryon content of our systems in Section 11 and X-ray underluminous systems in Section 12. Throughout this paper we assume a cosmology  $H_0 = 75 \text{ km s}^{-1} \text{ Mpc}^{-1}$ ,  $\Omega_M = 0.3$ , and  $\Omega_\Lambda = 0.7$  unless mentioned otherwise.

## 2. GROUP SAMPLE DEFINITION

### 2.1. Optically (Spectroscopically) Selected Groups

Our optical sample is selected from the Canadian Network for Observational Cosmology Field Galaxy Redshift Survey 2 (CNOC2), a survey consisting of four sky patches, roughly equally spaced in RA, with a total area of about  $1.5 \text{ deg}^{-2}$  (Carlberg et al. 1999).  $UBVRcI_c$  photometry of the patches yielded  $\sim 40,000$  galaxies above the survey’s  $R_c \simeq 23.0$  limit. Follow-up spectroscopy of these fields resulted in redshifts for over 6000 galaxies with a completeness of 48% down to  $R_c = 21.5$  (Yee et al. 2000). Groups present in the survey were then detected as pure galaxy overdensities in redshift space. In total, over 200 groups ranging in redshift  $0.12 < z < 0.55$  were detected (Carlberg et al. 2001). Given the optical spectroscopic wavelength range for CNOC2 spectroscopy, the effective redshift range for the full sample corresponds to the available wavelength range of the Ca II H and K spectral features.

Complementary to the existing spectroscopy, the GEEC has built up a multiwavelength data set, including *HST*-ACS, infrared, and UV imaging and X-ray data (described and utilized in the present analysis), in order to study galaxy groups in the CNOC2 fields in detail. Twenty-six of the CNOC2 groups at  $0.3 < z < 0.55$  have been actively targeted with Magellan-LDSS2 to improve the spectroscopic completeness and depth of the sample. Three hundred ninety-two unique LDSS2 redshifts were obtained in three of the four CNOC2 patches elevating the average completeness at the coordinates of the targeted groups to 74% above a limiting magnitude of  $R_c = 22$  (Wilman et al. 2005a). Ten groups (six in the RA14h field, and four in the RA21h) were observed with VLT-FORS2 in June and July of 2005. These data have recently been reduced and yielded 233 previously unknown redshifts and a magnitude limit of  $R = 23.2$  (Henderson 2010). Throughout this paper we consider only those 38 optical groups within the regions observed by the *XMM-Newton* + *Chandra* described in the next section, ensuring that the most direct comparisons between these differently identified systems are possible.

### 2.2. X-Ray-selected Groups

X-ray observations of two of the four CNOC2 fields were obtained and used to identify a comparison sample of X-ray-selected galaxy groups. These groups are selected from deep *XMM-Newton* + *Chandra* data in the RA14h and RA21h CNOC2 patches using a wavelet algorithm. A detailed discussion of their definition can be found in Finoguenov et al. (2009) but a brief overview follows. Note that since the publication of that paper, additional *XMM-Newton* data (ObsIDs 0603590101 and 060359020) of the RA21h field were acquired and are included here. The total area covered by the X-ray observations was 0.2 and 0.3  $\text{deg}^{-2}$  for the RA14h and RA21h fields, respectively. The total *XMM* exposure time for the RA21h field was 271.46 ks and the *Chandra* exposure time in this field was 101.88 ks. In the RA14h field, a total exposure time of 210.40 ks with *XMM* and 89.02 ks with *Chandra* were obtained.

For data from both instruments and patches, careful background and point source removal were performed and images

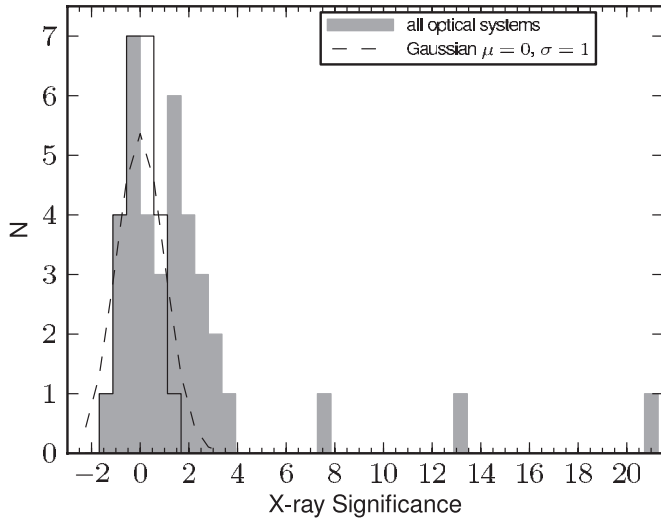


**Figure 1.** X-ray significance of optically selected systems. Black solid line indicates the negative portion of the histogram and its reflection above zero while the black dashed line shows a Gaussian approximation having a mean,  $\mu$ , of 0 and variance,  $\sigma$ , of 1.

co-added by normalizing each to account for the different sensitivity of the instruments to produce a joint exposure map. The combined maximum effective exposure times in units of the equivalent *Chandra* exposure at the center of the field are 691 ks for the RA21h patch and 469 ks for the RA14h patch. Wavelet reconstructions of the signal-to-noise (S/N) images for the co-added image and separate *XMM* and *Chandra* images were then produced and extended source detection carried out at 32'' and 64'' spatial scales. The positional uncertainty for the X-ray centers is of order of 10'' but can reach 30'' for low-significance sources. The total number of secure detections in the RA14h and RA21h patches is 31 and 33, respectively. An additional five sources with low significance (significance <2) are detected in each field.

### 3. X-RAY MEASUREMENTS

#### 3.1. Fluxes and Luminosities

For X-ray-selected systems, the X-ray flux is measured within an area defined via a wavelet reconstruction of the X-ray images to optimize the S/N for the source. Using the central positions and extents of the detections from the wavelet reconstructions, flux measurement was performed on the background and point source subtracted images. All X-ray sources have a wavelet detection  $\geq 4\sigma$ , corresponding to a certain detection in flux, but in cases where the aperture has been reduced in order to prevent merging of adjacent sources, the final measurement of significance may fall between 1 and 2. To ensure that we only include robust X-ray measurements, we choose to include X-ray-derived properties only for X-ray systems having a significance  $\geq 1$  in our analysis. Note that negative values of significance reflect that the measured flux is lower than the average background level. Statistical background removal sets the mean of the background to zero, while the statistical spread of actually observed counts results in a distribution around zero.

In order to measure the X-ray flux of our optical systems, we define a constant circular aperture, with a radius of 0.5, surrounding the *R*-band luminosity-weighted center of the group members. This aperture is derived from the confusion limit in the X-ray imaging. The distribution of the S/N of the X-ray

flux estimate (hereafter X-ray significance) estimated using the residual, background and point-source removed, image of our optical systems can be seen in Figure 1. The histogram is double peaked, with the first peak resulting from the noise in our flux measurements and the second the “real” peak of the X-ray significant systems. The noise peak can be approximated by a Gaussian having a mean of 0 and variance of 1 (shown as a dashed line). The solid line indicates the negative portion of the histogram and its reflection above zero. Comparison of this to the dashed, Gaussian approximation, line shows that the noise is slightly overestimated, and thus the significance underestimated. To help ensure the X-ray emission is real, we choose to include X-ray-derived properties only for optical systems having a significance  $\geq 2$  in our analysis.

The flux measurement is performed on background and point source subtracted *XMM* images only. The total flux for each group in the 0.5–2 keV band is computed as in Equation (1) of Finoguenov et al. (2007), extrapolating the surface brightness to  $r_{500}$  ( $\sim 0.6r_{200}$ ). The total flux and corresponding  $r_{200,X}$  are derived iteratively from the corrected observed flux using the redshift of the group (see Section 6.2) and appropriate scaling relations. Section 5.1 of Finoguenov et al. (2007) details these scaling relations. This includes extrapolation of the measured flux, assuming the surface brightness profile measured for local groups. For X-ray and optical systems with low X-ray significance, we calculate upper limits for the X-ray flux, radius, luminosity, and mass and these measures are demarcated by gray points in the appropriate relations. Note that we are unable to robustly measure X-ray temperatures for our systems given the depth of our data.

The rest-frame X-ray luminosity in the 0.1–2.4 keV band is calculated by *k*-correcting the flux measurement within  $r_{200,X}$  as described in Section 5.1 of Finoguenov et al. (2007) and is shown for our systems as a function of redshift in Figure 2. We can see from this figure and Figure 3 that, with increasing redshift, we are biased toward systems with higher X-ray luminosities and velocity dispersions.

#### 3.2. Apertures

To ensure that the assignment of a *constant* aperture centered on the luminosity-weighted group center for optical groups and a *variable* aperture centered on the X-ray emission peak for X-ray systems does not significantly bias our comparison, we first compare the flux measurements for groups which are independently detected both as optical and X-ray systems. There are only four such, relatively bright, systems having X-ray significance greater than our cutoff and which are not located near the X-ray and/or optical survey edges where luminosity-weighted centers can be particularly inaccurate and X-ray apertures incomplete. All four have higher X-ray fluxes for the X-ray-selected system than for the optical counterpart. On average, the difference is a factor of two, indicating that our choice of the 0.5 fixed aperture may lead to an underestimated flux despite the correction. In all these cases, the X-ray defined aperture is larger (up to a factor of two) than the 0.5. As the larger aperture is resulting in a larger flux this indicates that our systems likely have a flatter surface brightness profile than the applied assumed relation derived from local groups.

We then test the effect of using a constant aperture for all X-ray-selected systems, measuring the flux using the fixed 0.5 aperture but centered on the X-ray emission peak and calculating the difference between this measurement and the flux measured using the variable aperture. The average resultant percentage

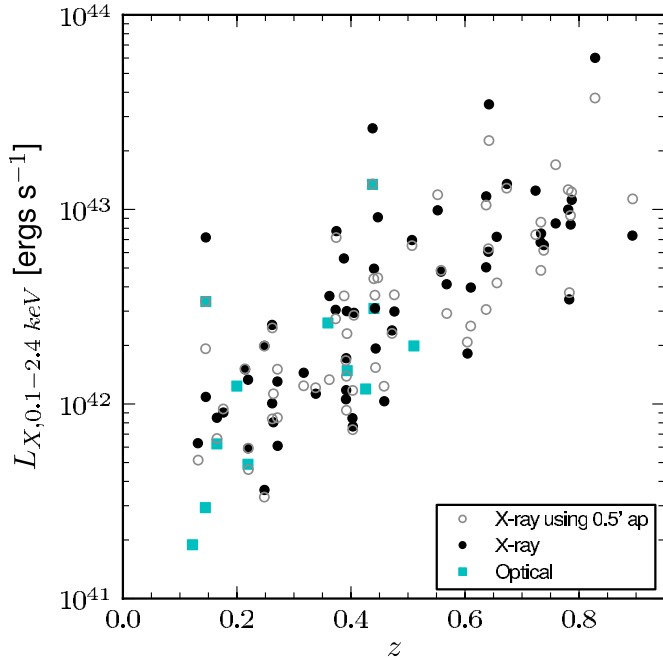


**Figure 2.** X-ray luminosity as a function of redshift for all X-ray (black circles) and optical (cyan squares) systems with X-ray significance  $\geq 1$  and 2, respectively. Note that  $2\sigma$  upper limits on X-ray luminosity for optical systems with low significance are not shown here. For X-ray systems, the X-ray luminosity derived using a fixed 0.5 aperture is shown in gray open circles. (A color version of this figure is available in the online journal.)

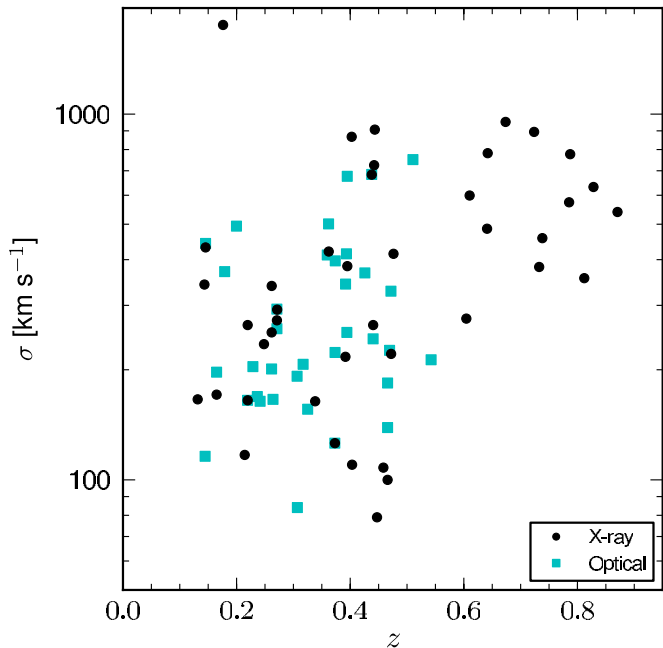


**Figure 3.** Velocity dispersion as a function of redshift given a  $\sigma$ -based  $r_{200}$  radial cut (see Section 6.5 for details) for all X-ray and optical systems. Note that upper limits on velocity dispersion are not shown here. (A color version of this figure is available in the online journal.)

change in the flux measures is less than 4% with measures scattered within a factor of two in both directions. We further find that X-ray flux measures can be greatly affected by the emission of neighboring groups. Since this “confusion” may bias measurement of flux, we flag systems which lie in crowded X-ray regions (see Section 6).

**Table 1**  
Summary of Supplemental Spectroscopy

	$\lambda$ Range ( $\text{\AA}$ )	FOV ( $'$ )	Field	$N_{\text{masks}}$	$N_{\text{spec}}$	$N_z$
IMACS	5000–9500 <sup>a</sup>	15.5 $\square$	RA14h	5	1197	553
			RA21h	2	551	312
FORS2	4300–7000	6.8 $\square$	RA14h	8	520	363
			RA21h	13	750	636
GMOS	5000–10000	5.5 $\square$	RA14h	3	125	115

**Notes.** Column description: instrument (Column 1), wavelength range (Column 2), field of view (Column 3), CNOC2 patch (Column 4), number of masks (Column 5), number of spectra (Column 6), total number of redshifts (Column 7). Note that for IMACS, the number of redshifts excludes stars.

<sup>a</sup> 4800–7800 for three of the RA14h field masks.

We conclude that for individual X-ray systems, the use of the 0.5 aperture may provide results more comparable to the optical systems but that, on average, the use of the X-ray aperture produces measures which are comparable to those resulting from a constant aperture but with higher S/N and less contamination. We thus choose to use this variable aperture for our X-ray systems. Figure 2 shows the X-ray luminosity (see Section 3) as a function of redshift for all systems and includes for the X-ray systems luminosities measured with both choices of aperture. The overall relation is very similar regardless of the choice of aperture. For the brightest X-ray systems, the use of the fixed aperture usually results in a noticeably lower  $L_X$ . This again indicates the applied local relation has a steeper surface brightness profile than our systems and implies that feedback may be more important in groups at higher redshift. This echoes the conclusion reached using the four matched systems that smaller X-ray apertures can lead to an underestimation of flux for bright systems and produces greater uncertainty in X-ray-derived properties.

#### 4. FOLLOW-UP SPECTROSCOPY

Although spectroscopic completeness is relatively high in areas containing most of our optically selected groups, the extended X-ray sources (our X-ray-selected systems) are often located in regions with very few previously determined redshifts. In many cases, a system redshift was impossible to determine from the available spectroscopy. A program of targeted follow-up spectroscopy for the X-ray detected systems was executed primarily using the VLT-FORS2 and Magellan-IMACS spectrographs. Objects brighter than  $R \approx 22$  and those close to the center of the X-ray contours were preferentially targeted. Some additional Gemini-GMOS spectroscopy has also been acquired as part of a program to extend this type of group study to higher redshift (Balogh et al. 2011b). A summary of the follow-up spectroscopy can be found in Table 1 and includes for each instrument the wavelength range and radius of the field of view (FOV) and the total number of masks, spectra, and redshifts for each field. In total 1946 previously unknown, secure redshifts have been measured, yielding a full sample of nearly 5000 redshifts in the RA14h and RA21h CNOC2 fields. We provide a sample of redshifts used in this analysis in Table 2 while the full catalog is available in the electronic version of this article.

##### 4.1. FORS2 Observations

FORS2 observations were conducted over the course of three visitor mode observing runs in 2007–2008, with corresponding

**Table 2**  
Spectroscopic Redshifts

R.A. (J2000)	Decl. (J2000)	$z$	Source	1 Mpc Group Member	$r_{200,\sigma}$ Group Member	$r_{200,X}$ Group Member
221.927383	9.147980	0.5685	GMOS	...	...	...
221.941650	9.159590	0.8850	GMOS	...	...	...
221.959946	9.192980	0.8497	GMOS	...	...	...
221.963501	9.136121	0.8112	GMOS	...	...	...
221.964722	9.137767	0.8116	GMOS	...	...	...
221.981888	9.151252	0.7233	GMOS	...	...	...
221.993881	9.211152	0.7040	GMOS	...	...	...
222.003189	9.144666	0.8836	GMOS	...	...	...
222.014923	9.215993	0.7014	GMOS	...	...	...
222.019150	8.903519	0.3581	CNOC2	...	...	...

**Notes.** Column description: object R.A. and decl. for equinox J2000.0 (Columns 1 and 2); object redshift (Column 3); source of object redshift (Column 4); X-ray and/or optical group(s) for which object is a member for 1 Mpc,  $r_{200,\sigma}$ , and  $r_{200,X}$  radial cuts (Columns 5–7). (This table is available in its entirety in a machine-readable form in the online journal. A portion is shown here for guidance regarding its form and content.)

run IDs of 080.A-0427(D) (0.6 night, 2007 October 5), 080.A-0427(B) (two half nights starting 2008 March 1), and 081.A-0103(B) (two half nights starting 2008 August 24) on one of the four 8.2 m Unit Telescopes of the Very Large Telescope array. A total of 21 (Mask eXchange Unit (MXU); multi-object) masks ( $6.8 \times 6.8$  FOV) were observed. Observations were obtained in both the RA14h and RA21h fields, and were designed to maximize the number of extended X-ray sources targeted and their membership. Slits were placed on galaxies with unknown redshifts, prioritizing galaxies close to the X-ray centers and with magnitudes  $R < 22$ , although fainter galaxies were used to fill the masks. A handful of objects with previously determined redshifts were also re-observed to allow for calibration.

The GRIS300V grism and GG375 filter were used, resulting in an effective wavelength range of  $\approx 430\text{--}700$  nm. A slit width of  $1''$  was used for all objects with a dispersion of  $1.68 \text{ \AA pixel}^{-1}$ . Slit lengths were set to  $\geq 5''$  in order to maximize the total number of objects per mask and obtain many redshifts in the central X-ray source regions where brightest group galaxies (BGGs) are likely to reside. The total integration time per mask ranged from 49 to 77 minutes.

#### 4.1.1. FORS2 Data Reduction

Reduction of the FORS2 data primarily involved a modification of the standard FORS2 pipeline procedure. The data calibration was performed with version 4.3.5 of the FORS pipeline which performs bias correction, flat-fielding, correction for optical distortions, and wavelength calibration (Appenzeller et al. 1998). The pipeline also detects and extracts individual object spectra and performs sky subtraction. However, the standard object detection and sky subtraction pipeline procedures are not ideal for our purposes. As no co-adding of exposures can be done using the pipeline, chip images from consecutive exposures were co-added using the Image Reduction and Analysis Facility (IRAF<sup>8</sup>) *imcombine* tool with cosmic-ray rejection applied before further pipeline reduction steps were applied. Sky subtraction was done in two ways: first, using a local (on slit) sky subtraction and then using a “global plus median” method. The latter produces a sky spectrum computed as the median

level of all the pixel values of all the CCD spectra in each wavelength bin renormalized after flat-fielding and the other initial processing steps. This method is the most robust as our small slit size and separation often causes spurious results for local subtraction. However, for large slits containing faint objects, local subtraction is superior and images processed in this way are used when measuring redshifts for such objects.

In order to determine redshifts, we adapted the ZSPEC software used by the DEEP2 redshift survey (Davis et al. 2003, 2007) for use with our FORS2 MXU data. In ZSPEC, spectra are first cross-correlated to eigen-templates (stellar, galaxy, and QSO templates) and the 10 best-fitted redshifts and  $\chi^2$  are provided. The spectra (both two and one dimensions) and their redshift fits were then visually examined in order to determine the correct redshift. Usually the first or second best  $\chi^2$  fit provided is a good fit. Instances where artifacts from sky line subtraction confuse the fitting, the S/N of the spectrum is relatively low, only a single emission line is detected, the spectrum is relatively featureless, or a bad pixel column exists often result in the first or second ranked fits being incorrect. In these cases, the appropriate solution often appears in a fit with a lower  $\chi^2$ . When none of the ten choices is a good match, any spectral features easily identified by eye were used to identify a probable redshift, which could be confirmed by manual cross-correlation.

Objects without a successful redshift determination were re-evaluated with additional information, such as object magnitude and slit position which can indicate, for example, that a redshift is unlikely to be obtainable or, in the case of very bright objects a stellar template is preferable, in a final attempt to establish a redshift. However, most objects for which we could not measure redshifts were very faint or—in the case of very bright objects—in an area where sky subtraction was not robust or where extraction was compromised due to slit edge proximity. At this stage, template fits were possible for the majority of all FORS2 objects ( $\sim 970/1270$ ). Finally, redshifts were assigned a quality flag to reflect the stellar or galactic nature of the object and the confidence of the redshift measurement. In this analysis we use only the best-quality redshifts, excluding objects with ambiguous fits. In total, 780 high-quality galaxy redshifts were obtained. Comparing to CNOC2 and IMACS redshift measurements from duplicate observations, we find a typical error of  $100 \text{ km s}^{-1}$  for our FORS2 redshifts.

<sup>8</sup> IRAF is distributed by the National Optical Astronomy Observatory, which is operated by the Association of Universities for Research in Astronomy, Inc., under cooperative agreement with the National Science Foundation.

## 4.2. IMACS Observations

We also obtained spectroscopy for both fields using Magellan-IMACS. The large FOV and close slit placement capability make the IMACS instrument excellent for observing galaxy groups at intermediate redshift in general and, specifically, its 15' FOV is an excellent match to that of *XMM* and thus to our X-ray-selected systems follow-up. Two multi-object masks of the RA14h field were observed in 2007 July 17–18 on the Baade/Magellan I 6.5 m telescope. These were taken with a grism of 200 lines  $\text{mm}^{-1}$ , giving a wavelength range of  $\approx 5000\text{--}9500 \text{ \AA}$  and a dispersion of  $2.0 \text{ \AA pixel}^{-1}$ . A slit width of  $1''$  was used and the exposure time was two hours for both masks. For these observations, the WB4800-7800 filter was used. These observations were made under relatively poor conditions, namely, significant moon. This, and the restricted wavelength range produced by the filter applied, lowered the overall redshift determination success rate for these masks. A further three masks in the RA14h field and two in the RA21h field were obtained in 2009 May 18–22 all with similar setup but without this filter.

### 4.2.1. IMACS Data Reduction

IMACS data were reduced using the Carnegie Observatories System for MultiObject Spectroscopy (COSMOS<sup>9</sup>) package. First, overscan regions of the CCDs were used to measure and subtract the bias level. Dome-flat exposures taken during the night were used to flat-field the data. Sky subtraction was performed using the method outlined by Kelson (2003). Wavelength calibrations were determined from HeNeAr arc exposures.

Redshifts for the IMACS spectra were determined from cross-correlating the flux-calibrated object spectra with input model templates. The routine adopts Sloan Digital Sky Survey (SDSS) spectral templates for early-type (SDSS template 24) and late-type galaxies (28) as input models and determines the best-fit redshift based on matching absorption and emission line features. The best-fit redshifts returned from the routine was then visually inspected to verify the object's redshift. For some objects, a good template fit was not found by the automatic routine, but spectral features were clearly visible in the galaxy spectrum. In these cases, we performed a manual cross-correlation to determine the redshift. In total, 865 high-quality galaxy redshifts, with errors of  $140 \text{ km s}^{-1}$ , were obtained from the IMACS observations.

### 4.3. Additional Spectroscopy

Finally, a single group in the RA14h field (XR14h03) was recently targeted with GMOS-S as part of an ongoing study of galaxy groups within the redshift range  $0.85 < z < 1$  (PI: Balogh). Slit widths were set to  $1''$  and an R600 grism with OG515 order blocking filter used. The spectroscopy was obtained in nod & shuffle mode (Glazebrook & Bland-Hawthorn 2001), nodding the telescope by  $\pm 0''.725$  from the center of the slit, every 60 s with a total exposure time of two hours per group target. All data were reduced in IRAF, using the GEMINI packages with minor modifications. See Balogh et al. (2011b) for further details of these observations and the data reduction. In total, 83 high-quality galaxy redshifts with errors of  $100 \text{ km s}^{-1}$  were obtained.

<sup>9</sup> <http://obs.carnegiescience.edu/Code/cosmos>

## 5. NIR PHOTOMETRY AND STELLAR MASS

### 5.1. NIR Observations

Details of the near-infrared  $K_s$  observations of the CNOC2 fields from SOFI on the New Technology Telescope (NTT) and Ingrid on the William Herschel Telescope (WHT) can be found in Balogh et al. (2009). These observations however did not cover much of the area with X-ray coverage (in particular much of the RA21h field) and so we have also obtained data with the WIRCam (Wide-field InfraRed Camera) on the Canada–France–Hawaii Telescope (CFHT). These data are described by McGee et al. (2011) but a brief description follows here. Four pointings were made for each of the two fields with each pointing having 33 minutes of exposure time. Each pointing was dithered in a five-point pattern to fill in the chip gaps and divided into 80 exposures of 25 s each. The resulting coverage area is  $30' \times 30'$  per field. These data were subsequently reduced and processed by the Terapix pipeline.

### 5.2. Galaxy Stellar Masses

Stellar masses for our galaxies were computed by template-fitting their spectral energy distributions (SEDs), using available photometry, as in McGee et al. (2011). A summary of this stellar mass derivation follows. The observed photometry, typically including  $K, i, r, g, u$ , *Galaxy Evolution Explorer* (GALEX) NUV and FUV, was compared to a large grid of model SEDs constructed using the Bruzual & Charlot (2003) stellar population synthesis code and assuming a Chabrier initial mass function (IMF; Chabrier 2003). This grid of models uniformly samples the allowed parameters of formation time, galaxy metallicity, and the dual component Charlot & Fall (2000) dust model and, as in Salim et al. (2007), the star formation history of a galaxy is assumed to be represented by an exponential model augmented with starbursts. Model magnitudes at nine redshift bins between 0.25 and 0.6 were derived by convolving these model SEDs with the observed photometric bandpasses.  $\chi^2$  is minimized while summing over all the models at the redshift of the galaxy and taking the observed uncertainty on each point into account. Comparison to other estimates of stellar mass shows  $1\sigma$  uncertainties of the order 0.15 dex.

## 6. MEASURING GROUP PROPERTIES

The global properties of our X-ray and optically selected groups are presented in Tables 3–6. Table 3 lists the group identification number for the X-ray system (Column 1); IAU name (Column 2); R.A. and decl. of the center of the extended X-ray emission for Equinox J2000.0 (Columns 3 and 4); spectroscopic redshift (Column 5); group redshift quality (Column 6); the total flux in the 0.5–2 keV band (Column 7); and significance of the X-ray flux (Column 8). Table 4 lists the lists the group identification number for the X-ray system (Column 1); number of member galaxies within 1 Mpc (Column 2); the radius in arcseconds of 1 Mpc (Column 3); the velocity dispersion within a 1 Mpc cut (Column 4); spectroscopic completeness (to  $R < 22$ ) within a 1 Mpc cut (Column 5), dynamical complexity within a 1 Mpc cut (Column 6); the number of member galaxies within a  $\sigma$ -derived  $r_{200}$  ( $r_{200,\sigma}$ ) (Column 7); the radius,  $r_{200,\sigma}$ , in arcseconds (Column 8); the velocity dispersion within  $r_{200,\sigma}$  (Column 9); spectroscopic completeness (to  $R < 22$ ) within  $r_{200,\sigma}$  (Column 10), dynamical complexity within  $r_{200,\sigma}$  (Column 11); the number of member galaxies within an X-ray-derived  $r_{200}$  (Column 12); the radius,  $r_{200,X}$ , in arcseconds (Column 13);

**Table 3**  
Basic Properties of X-Ray-selected Groups

XID	IAU Name	R.A. (J2000)	Decl. (J2000)	$z$	$Q$	X-Ray Flux ( $10^{-14}$ erg $\text{cm}^{-2}$ )	X-Ray Significance
XR14h02	144949+0910.9	222.45584	+9.18167	0.1315	1.0	$0.89 \pm 0.31$	2.84
XR14h09	145009+0904.3	222.54075	+9.07188	0.6420	1.0	$1.23 \pm 0.12$	9.75
XR14h10	144905+0905.5	222.27293	+9.09198	0.7382	1.0	$0.13 \pm 0.05$	2.48
XR21h08	215143-0526.0	327.93324	-5.43371	0.2617	1.0	$0.77 \pm 0.10$	7.74
XR21h10	215045-0530.9	327.68966	-5.51535	0.3383	1.0	$0.17 \pm 0.05$	3.23
XR21h11	215111-0535.6	327.79834	-5.59362	0.4762	1.0	$0.20 \pm 0.04$	4.5
XR21h12	215136-0535.8	327.90274	-5.59811	0.2195	1.0	$0.25 \pm 0.08$	3.2
XR21h14	215041-0541.0	327.67186	-5.68486	0.4379	1.0	$2.34 \pm 0.08$	26.24
XR21h15	215144-0540.3	327.93620	-5.67284	0.7326	1.0	$0.14 \pm 0.05$	2.69
XR21h60	215014-0545.7	327.55853	-5.76198	0.3171	1.0	$0.27 \pm 0.06$	4.14
XR21h64	215036-0550.4	327.65308	-5.84050	0.2482	1.0	$0.68 \pm 0.13$	5.17
XR21h09	215137-0530.7	327.90525	-5.51241	0.2195	1.5	$0.61 \pm 0.08$	7.47
XR14h03	144910+0910.5	222.29202	+9.17579	0.7872	2.0	$0.20 \pm 0.05$	3.53
XR14h08	145007+0906.6	222.53225	+9.11101	0.5070	2.0	$0.41 \pm 0.09$	4.22
XR14h18	145021+0901.3	222.58939	+9.02196	0.3731	2.0	$0.39 \pm 0.12$	3.01
XR14h22	144934+0854.9	222.39582	+8.91603	0.2714	2.0	$0.16 \pm 0.07$	2.14
XR14h25	144912+0849.8	222.30276	+8.83071	0.2710	2.0	$0.36 \pm 0.10$	3.56
XR14h35	144954+0903.2	222.47810	+9.05440	0.6409	2.0	$0.18 \pm 0.05$	3.23
XR14h40	144958+0859.3	222.49465	+8.98870	0.6370	2.0	$0.15 \pm 0.09$	1.66
XR14h44	144909+0855.2	222.28837	+8.92101	0.6102	2.0	$0.13 \pm 0.05$	2.61
XR21h06	215124-0525.7	327.85298	-5.42894	0.1454	2.0	$1.26 \pm 0.18$	6.81
XR21h07	215124-0527.1	327.85378	-5.45297	0.1454	2.0	$8.18 \pm 0.18$	44.98
XR21h13	215100-0538.0	327.75085	-5.63451	0.2483	2.0	$0.11 \pm 0.07$	1.49
XR21h18	215026-0546.2	327.60980	-5.77096	0.3916	2.0	$0.12 \pm 0.04$	2.66
XR21h20	215111-0548.5	327.79831	-5.80904	0.1434	2.0	<0.42	-0.34
XR21h23	214956-0556.8	327.48498	-5.94810	0.3876	2.0	$0.65 \pm 0.17$	3.85
XR21h31	215202-0533.9	328.01069	-5.56647	0.4584	2.0	$0.07 \pm 0.06$	1.11
XR21h32	215027-0544.3	327.61643	-5.73947	0.7334	2.0	$0.16 \pm 0.03$	4.74
XR21h33	215029-0547.0	327.62119	-5.78424	0.3916	2.0	$0.19 \pm 0.08$	2.18
XR21h37	215046-0528.8	327.69397	-5.48061	0.4433	2.0	$0.15 \pm 0.04$	3.56
XR21h42	215105-0539.9	327.77157	-5.66557	0.4033	2.0	$0.07 \pm 0.03$	1.97
XR21h50	215115-0546.8	327.81375	-5.78166	0.5678	2.0	$0.17 \pm 0.08$	2.19
XR21h55	215132-0533.6	327.88562	-5.56036	0.2618	2.0	$0.30 \pm 0.06$	4.81
XR14h11	144927+0904.4	222.36371	+9.07427	0.4720	2.5	$0.16 \pm 0.04$	3.51
XR14h12	144940+0902.7	222.41983	+9.04645	0.1648	2.5	$0.74 \pm 0.17$	4.22
XR14h19	144933+0859.9	222.38956	+8.99939	0.6372	2.5	$0.38 \pm 0.05$	6.82
XR14h29	144939+0912.2	222.41519	+9.20452	0.3622	2.5	$0.49 \pm 0.11$	4.46
XR14h33	144936+0908.2	222.40358	+9.13817	0.8120	2.5	<0.35	-0.13
XR21h27	215117-0523.6	327.82295	-5.39383	0.1762	2.5	$0.70 \pm 0.14$	4.99
XR14h01	144940+0847.8	222.41731	+8.79825	0.3745	3.0	$0.98 \pm 0.13$	7.29
XR14h05	144915+0907.9	222.31547	+9.13188	0.7853	3.0	$0.15 \pm 0.05$	2.93
XR14h07	145018+0906.9	222.57809	+9.11531	0.5521	3.0	$0.47 \pm 0.14$	3.35
XR14h13	144957+0904.6	222.48963	+9.07809	0.5580	3.0	$0.21 \pm 0.07$	2.95
XR14h23	144853+0853.9	222.22288	+8.89904	0.8282	3.0	$1.19 \pm 0.09$	12.63
XR14h24	144914+0851.0	222.30994	+8.85140	1.0114	3.0	$0.18 \pm 0.04$	3.95
XR14h26	144948+0854.5	222.45019	+8.90837	0.7810	3.0	$0.18 \pm 0.09$	2.07
XR14h37	145016+0859.5	222.56919	+8.99258	0.5567	3.0	<0.23	0.34
XR14h38	145007+0859.3	222.52976	+8.99000	0.2968	3.0	<0.61	-0.02
XR14h39	144944+0859.4	222.43683	+8.99109	0.2639	3.0	$0.23 \pm 0.21$	1.1
XR14h41	144915+0857.7	222.31469	+8.96299	0.8936	3.0	$0.08 \pm 0.03$	2.53
XR14h47	144904+0853.0	222.26735	+8.88464	0.4053	3.0	$0.30 \pm 0.08$	3.48
XR21h16	215021-0541.2	327.58912	-5.68771	0.3912	3.0	$0.11 \pm 0.05$	2.08
XR21h17	215004-0546.3	327.51681	-5.77184	0.7828	3.0	$0.05 \pm 0.04$	1.14
XR21h19	215115-0548.0	327.81629	-5.80110	0.5674	3.0	<0.12	0.91
XR21h21	215018-0550.1	327.57591	-5.83644	0.4404	3.0	$0.42 \pm 0.08$	5.14
XR21h30	215047-0533.8	327.69873	-5.56387	0.3949	3.0	<0.07	0.13
XR21h40	215011-0548.0	327.54848	-5.80150	0.6556	3.0	$0.21 \pm 0.06$	3.45
XR21h41	215011-0552.9	327.54919	-5.88323	0.8705	3.0	<0.15	0.77
XR21h43	215028-0542.1	327.61959	-5.70213	0.6044	3.0	$0.05 \pm 0.03$	1.47
XR21h48	215111-0544.1	327.79699	-5.73500	0.2613	3.0	<0.16	0.52
XR21h49	215101-0544.5	327.75567	-5.74279	0.4026	3.0	$0.08 \pm 0.05$	1.47
XR21h59	215122-0541.1	327.84397	-5.68637	0.4421	3.0	$0.26 \pm 0.06$	4.29
XR21h69	215016-0555.9	327.56980	-5.93195	0.6735	3.0	$0.39 \pm 0.08$	4.58

**Table 3**  
(Continued)

XID	IAU Name	R.A. (J2000)	Decl. (J2000)	$z$	$Q$	X-Ray Flux ( $10^{-14}$ erg $\text{cm}^{-2}$ )	X-Ray Significance
XR14h04	144932+0910.6	222.38352	+9.17669	0.2143	3.5	$0.72 \pm 0.15$	4.74
XR14h14	144857+0902.4	222.24015	+9.04137	0.7237	3.5	$0.30 \pm 0.05$	5.21
XR21h22	215115-0552.8	327.81317	-5.88123	0.7590	3.5	$0.17 \pm 0.09$	1.89
XR21h67	215109-0553.2	327.79085	-5.88775	0.4472	3.5	$0.74 \pm 0.13$	5.49

**Notes.** Column description: group identification number for the X-ray system (Column 1); IAU name (Column 2); R.A. and decl. of the center of the extended X-ray emission for equinox J2000.0 (Columns 3 and 4); spectroscopic redshift (Column 5); group redshift quality (Column 6); the total flux in the 0.5–2 keV band (Column 7); and significance of the X-ray flux (Column 8).

velocity dispersion within  $r_{200,X}$  (Column 14); spectroscopic completeness (to  $R < 22$ ) within  $r_{200,X}$  (Column 15), and the dynamical complexity within  $r_{200,X}$  (Column 16). Tables 5 and 6 tabulate the optical groups and are similarly structured, classifying them according to the group number from the optically selected group catalog of Carlberg et al. (2001) and with an additional column in Table 5 (Column 5) listing the X-ray group ID where there is a confident match.

In total, our sample contains 39 high-quality X-ray and 38 optical systems. Note that IAU names for several groups in the RA21h field have changed since the publication of Paper I as a result of improved centers due to the addition of *XMM* data in that field. Two of our high-quality systems have low ( $<1$ ) X-ray significance. The original significance of these systems was sufficient to occasion targeting for follow-up spectroscopy but was subsequently lessened with the addition of X-ray data and modifications to the X-ray reductions. As follow-up spectroscopy yielded groups with secure redshifts, we choose to include them in our sample, but do not include their X-ray-derived properties in our analysis. Twelve of our optically selected systems have significant X-ray emission when a fixed aperture is placed at the optical center.

### 6.1. Matched X-Ray–Optical Systems

Examining the redshifts and proximity on the sky of groups in both samples, nine of our optically selected systems are associable with X-ray systems but five of these have an X-ray significance  $<2$  using the optical center and aperture. Several of our optically selected systems do have significant X-ray emission but are not readily matched to X-ray systems. Recall that the latter require a  $\geq 4\sigma$  detection on the wavelet images in order to be identified. It is important to note that this is projected X-ray emission and thus absolute certainty in assigning X-ray emission to an optically detected system is not possible. The following sections describe the assignment of redshift and members to all systems as well as the calculation of dynamical mass.

### 6.2. X-Ray-selected Group Redshifts

Initial group redshifts for X-ray systems were established by examining objects within and around the immediate vicinity of the contours defining the extended X-ray sources. An obvious clustering of galaxies in both redshift and projected spatial coordinates was often obvious and in some cases a prominent galaxy, possibly the BGG, exists near the X-ray center. Each group was assigned a redshift and a corresponding quality flag reflecting its plausibility. These quality flags are not related to those for individual galaxy redshifts and range from 1 to 3, from highest to lowest quality. A quality of 1 reflects complete

confidence in the redshift assignment and significant X-ray emission while a quality of 2 indicates a fairly confident redshift but low-significance X-ray emission, weak multiple clustering, or a highly incomplete region within the group (either an extended gap in the survey area or a few bright objects near the group center without redshifts). A quality of flag 3 indicates a highly questionable redshift due to the projection of strong multiple clustering (more than 1 redshift at which galaxies are grouped), very low significance X-ray emission, or a dearth of objects with redshifts in the area. We add 0.5 to the quality flag of any group in regions of “confused” emission: where X-ray contours overlap. This does *not* indicate a lesser certainty in the redshift/overall quality of the group. In this paper, we will often refer to subsets of X-ray systems as quality 1 and as quality 1 & 2, ignoring the 0.5 flag. This flag, and information about a system’s dynamical complexity (see Section 8), allows us to explore underlying reasons for outliers from our relations.

In cases of more than one plausible group redshift, we apply our membership finding algorithm with all possible solutions to find the most self-consistent solution. Recall that we are always examining projected X-ray emission and that, as in assigning X-ray emission to previously defined optical systems, assigning a group redshift and galaxy members to X-ray emission cannot be done with 100% confidence. The difficulty can be illustrated in part by the existence of such a large number of quality 3 groups in our sample many of which are classified as such due to the presence of galaxy clustering at different redshifts.

### 6.3. Group Membership

Details of our membership finder algorithm are found in Wilman et al. (2005a) but a basic description, with changes made for the current analysis, follows. Beginning with the X-ray center and redshift for each group, an initial velocity dispersion of  $500 \text{ km s}^{-1}$  is assumed and a maximum redshift offset  $\delta(z)_{\text{max}}$  calculated to clip members at  $2\times$  the velocity dispersion. This is then converted into a spatial offset  $\delta(\theta)_{\text{max}}$  which is within  $1/10$  the equivalent distance to  $\delta(z)_{\text{max}}$  in the line-of-sight direction, and group members are selected by applying these redshift and spatial limits as follows:

$$\delta(r)_{\text{max}} = \frac{1}{10} \frac{\delta(z)_{\text{max}}}{h_{75}^{-1} \text{ Mpc}} \quad (1)$$

$$\delta(\theta)_{\text{max}} = 206265'' \frac{\delta(r)_{\text{max}}}{h_{75}^{-1} \text{ Mpc}} \left( \frac{D_{\theta}}{h_{75}^{-1} \text{ Mpc}} \right)^{-1}, \quad (2)$$

where 10 is the aspect ratio and the angular diameter distance  $D_{\theta}$  is a function of redshift. Note to tune this offset limit to our X-ray-selected group sample, allowing for distinction between



**Table 4**  
Measured Properties of X-Ray-selected Groups

XID	$N$ 1 Mpc	Radius ( $''$ )	$\sigma$ ( $\text{km s}^{-1}$ )	Completeness $R < 22$	Dynamical Complexity	$N$ $r_{200,\sigma}$	Radius ( $''$ )	$\sigma$ ( $\text{km s}^{-1}$ )	Completeness $R < 22$	Dynamical Complexity	$N$ $r_{200,X}$	Radius ( $''$ )	$\sigma$ ( $\text{km s}^{-1}$ )	Completeness $R < 22$	Dynamical Complexity
XR14h02	12	455.97	$213 \pm 33$	0.61	...	7	164.88	$166 \pm 58$	0.63	...	7	204.84	$166 \pm 58$	0.63	...
XR14h09	15	155.01	$850 \pm 112$	0.67	AD	20	196.65	$782 \pm 88$	0.67	AD,DS	13	117.72	$817 \pm 141$	0.67	AD
XR14h10	5	146.62	$458 \pm 184$	0.93	...	5	103.01	$458 \pm 184$	0.94	...	4	73.08	$483 \pm 308$	1.00	...
XR21h08	14	263.99	$262 \pm 38$	0.37	...	9	135.30	$253 \pm 54$	0.45	...	11	147.96	$280 \pm 46$	0.41	...
XR21h10	11	221.08	$241 \pm 35$	0.62	...	4	70.40	$164 \pm 190$	0.67	...	4	99.00	$164 \pm 190$	0.70	...
XR21h11	14	179.72	$374 \pm 75$	0.61	AD	11	133.64	$415 \pm 86$	0.68	...	10	90.72	$428 \pm 87$	0.69	...
XR21h12	37	301.07	$255 \pm 32$	0.58	...	11	165.52	$265 \pm 78$	0.61	...	11	126.72	$265 \pm 78$	0.62	...
XR21h14	46	188.35	$750 \pm 73$	0.69	AD	58	235.72	$683 \pm 60$	0.69	AD	37	154.44	$704 \pm 81$	0.67	...
XR21h15	4	147.04	$382 \pm 289$	0.61	...	4	86.45	$382 \pm 289$	0.73	...	4	74.16	$382 \pm 289$	0.75	...
XR21h60	5	230.88	$<156$	0.45	...	0	...	...	...	...	3	110.52	$107 \pm 129$	0.43	...
XR21h64	5	274.42	$179 \pm 52$	0.45	...	3	131.59	$235 \pm 285$	0.38	...	3	146.88	$235 \pm 285$	0.38	...
XR21h09	26	301.08	$256 \pm 36$	0.48	...	10	102.92	$165 \pm 34$	0.72	...	12	150.48	$213 \pm 41$	0.64	...
XR14h03	7	143.21	$860 \pm 213$	0.79	...	10	165.58	$777 \pm 215$	0.76	AD	3	77.40	$899 \pm 575$	0.67	...
XR14h08	7	173.75	$104 \pm 126$	0.70	...	5	31.46	$<102$	0.83	...	6	102.60	$98 \pm 133$	0.70	...
XR14h18	7	207.63	$151 \pm 73$	0.58	...	4	49.79	$126 \pm 144$	0.80	...	6	112.32	$174 \pm 76$	0.68	...
XR14h22	20	257.20	$382 \pm 42$	0.73	DS	9	151.65	$292 \pm 76$	0.85	...	6	105.48	$233 \pm 77$	0.94	...
XR14h25	22	257.82	$267 \pm 43$	0.55	DS	13	141.65	$273 \pm 56$	0.67	...	11	124.20	$285 \pm 67$	0.64	...
XR14h35	6	155.32	$557 \pm 153$	0.64	...	3	122.57	$486 \pm 454$	0.59	...	3	81.36	$486 \pm 454$	0.79	...
XR14h40	3	155.66	$<299$	0.70	...	3	75.64	$<298$	0.88	...	3	78.48	$<292$	0.88	...
XR14h44	11	158.66	$599 \pm 91$	0.70	AD,DS	11	157.30	$599 \pm 91$	0.72	AD,DS	5	72.00	$426 \pm 423$	0.92	...
XR21h06	50	419.22	$426 \pm 46$	0.39	...	49	389.95	$432 \pm 46$	0.40	...	16	107.64	$466 \pm 93$	0.53	...
XR21h07	46	419.27	$443 \pm 47$	0.40	...	0	...	...	...	...	40	313.56	$473 \pm 49$	0.46	...
XR21h13	6	274.48	$<100$	0.66	...	5	55.95	$<100$	0.86	...	5	102.24	$<100$	0.69	...
XR21h18	11	201.48	$244 \pm 53$	0.59	AD	0	...	...	...	...	7	88.20	$217 \pm 57$	0.68	...
XR21h20	17	424.23	$362 \pm 70$	0.49	...	15	313.95	$342 \pm 79$	0.52	...	$\leq 5$	$<168.84$	$164 \pm 119$	0.64	...
XR21h23	4	202.68	$467 \pm 539$	0.56	...	0	...	...	...	...	3	123.84	$<100$	0.65	...
XR21h31	7	183.63	$127 \pm 33$	0.38	...	3	36.06	$108 \pm 121$	0.83	...	5	74.52	$66 \pm 100$	0.60	...
XR21h32	5	146.97	$<138$	...	...	2	52.54	$<232$	...	...	3	75.60	$<222$	...	...
XR21h33	8	201.40	$198 \pm 58$	0.60	...	7	82.25	$217 \pm 57$	0.81	...	7	95.40	$217 \pm 57$	0.78	...
XR21h37	25	186.76	$864 \pm 94$	0.55	AD	34	309.39	$907 \pm 91$	0.40	AD,DS	17	88.20	$917 \pm 118$	0.81	...
XR21h42	7	197.77	$103 \pm 61$	0.69	...	4	41.00	$110 \pm 120$	1.00	...	4	78.12	$110 \pm 120$	0.64	...
XR21h50	8	164.11	$470 \pm 192$	0.57	...	0	...	...	...	...	4	83.16	$201 \pm 223$	0.63	...
XR21h55	13	264.04	$339 \pm 81$	0.55	...	10	181.54	$339 \pm 101$	0.63	...	7	121.32	$392 \pm 147$	0.63	...
XR14h11	18	180.65	$331 \pm 55$	0.78	AD,DS	6	71.57	$221 \pm 70$	0.82	...	6	87.12	$221 \pm 70$	0.75	...
XR14h12	9	378.08	$191 \pm 88$	0.70	...	5	138.25	$171 \pm 188$	0.74	...	6	177.48	$197 \pm 131$	0.73	...
XR14h19	2	155.59	$<194$	...	...	0	...	...	...	...	2	93.96	$<194$	...	...
XR14h29	16	211.48	$428 \pm 68$	0.67	...	15	170.58	$421 \pm 73$	0.74	...	10	119.52	$496 \pm 112$	0.67	...
XR14h33	3	141.78	$356 \pm 318$	0.71	...	3	73.95	$356 \pm 318$	0.70	...	$\leq 3$	$<84.24$	$356 \pm 318$	0.67	...

**Table 4**  
(Continued)

XID	$N$ 1 Mpc	Radius ( $''$ )	$\sigma$ ( $\text{km s}^{-1}$ )	Completeness $R < 22$	Dynamical Complexity	$N$ $r_{200,\sigma}$	Radius ( $''$ )	$\sigma$ ( $\text{km s}^{-1}$ )	Completeness $R < 22$	Dynamical Complexity	$N$ $r_{200,X}$	Radius ( $''$ )	$\sigma$ ( $\text{km s}^{-1}$ )	Completeness $R < 22$	Dynamical Complexity
XR21h27	9	360.67	$1199 \pm 282$	0.37	...	42	1350.54	$1753 \pm 143$	0.33	AD,DS	7	172.08	$695 \pm 219$	0.47	...
XR14h01	6	207.09	$<109$	0.27	...	0	...	...	...	...	5	136.80	$<147$	0.17	...
XR14h05	4	143.39	$574 \pm 359$	0.64	...	4	122.68	$574 \pm 359$	0.63	...	2	72.72	$634 \pm \dots$	...	...
XR14h07	2	166.37	$<211$	...	...	2	60.21	$<211$	...	...	2	102.96	$<210$	...	...
XR14h13	1	165.50	...	...	...	0	...	...	...	...	1	87.12	...	...	...
XR14h23	4	140.87	$632 \pm 80$	...	...	4	129.22	$632 \pm 80$	...	...	4	105.84	$632 \pm 80$	...	...
XR14h24	2	133.33	$205 \pm \dots$	...	...	0	...	...	...	...	2	69.48	$205 \pm \dots$	...	...
XR14h26	6	143.64	$205 \pm 94$	0.70	...	0	...	...	...	...	4	75.96	$130 \pm 163$	0.69	...
XR14h37	8	165.69	$461 \pm 169$	0.59	...	2	90.81	$<321$	...	...	$\leq 3$	$<88.92$	$295 \pm 352$	0.60	...
XR14h38	1	241.47	...	...	...	0	...	...	...	...	$\leq 1$	$<133.92$	...	...	...
XR14h39	2	262.34	$72 \pm \dots$	...	...	0	...	...	...	...	1	114.84	...	...	...
XR14h41	2	137.64	$<283$	...	...	2	54.44	$<283$	...	...	2	63.00	$<295$	...	...
XR14h47	1	197.22	...	...	...	0	...	...	...	...	1	141.48	...	...	...
XR21h16	10	201.39	$311 \pm 75$	0.44	...	0	...	...	...	...	2	86.04	$64 \pm \dots$	...	...
XR21h17	4	143.56	$228 \pm 158$	0.42	...	0	...	...	...	...	3	60.48	$74 \pm 162$	0.67	...
XR21h19	6	164.16	$329 \pm 221$	0.59	...	0	...	...	...	...	$\leq 6$	$<77.40$	$329 \pm 221$	0.69	...
XR21h21	20	187.90	$309 \pm 49$	0.59	...	9	91.22	$265 \pm 40$	0.64	...	10	108.00	$294 \pm 48$	0.65	...
XR21h30	4	200.37	$384 \pm 276$	0.56	...	4	144.46	$384 \pm 276$	0.61	...	$\leq 2$	$<78.48$	$575 \pm \dots$	...	...
XR21h40	2	153.63	$383 \pm \dots$	...	...	0	...	...	...	...	1	82.80	...	...	...
XR21h41	2	138.71	$540 \pm \dots$	...	...	2	106.14	$540 \pm \dots$	...	...	$\leq 2$	$<70.92$	$540 \pm \dots$	...	...
XR21h43	4	159.36	$276 \pm 177$	0.74	...	4	73.20	$276 \pm 177$	0.90	...	3	66.24	$206 \pm 249$	0.89	...
XR21h48	7	263.47	$159 \pm 120$	0.54	...	2	75.97	$<142$	...	...	$\leq 2$	$<108.00$	$<143$	...	...
XR21h49	12	198.20	$745 \pm 141$	0.53	...	26	320.96	$867 \pm 99$	0.60	AD	1	79.92	...	...	...
XR21h59	10	187.32	$689 \pm 136$	0.68	...	12	248.35	$725 \pm 134$	0.64	...	4	97.92	$798 \pm 369$	0.76	...
XR21h69	4	151.92	$952 \pm 498$	0.46	...	5	230.46	$952 \pm 156$	0.46	...	1	92.52	...	...	...
XR14h04	6	306.54	$156 \pm 49$	0.67	...	3	74.50	$117 \pm 132$	1.00	...	3	158.04	$117 \pm 132$	0.68	...
XR14h14	8	147.72	$951 \pm 360$	0.62	...	9	204.01	$894 \pm 316$	0.60	...	5	85.68	$761 \pm 281$	0.63	...
XR21h22	2	145.24	$533 \pm \dots$	...	...	0	...	...	...	...	1	75.24	...	...	...
XR21h67	6	186.20	$80 \pm 68$	0.43	...	0	...	...	...	...	4	121.32	$79 \pm 46$	0.54	...

**Notes.** Column description: group identification number for the X-ray system (Column 1); number of member galaxies within 1 Mpc (Column 2); the radius in arcseconds of 1 Mpc (Column 3); the velocity dispersion within a 1 Mpc cut (Column 4); spectroscopic completeness (to  $R < 22$ ) within a 1 Mpc cut (Column 5), dynamical complexity within a 1 Mpc cut (Column 6); the number of member galaxies within a  $\sigma$ -derived  $r_{200}$  (Column 7); the radius in arcseconds of a  $\sigma$ -derived  $r_{200}$  (Column 8); the velocity dispersion within a  $\sigma$ -derived  $r_{200}$  (Column 9); spectroscopic completeness (to  $R < 22$ ) within a  $\sigma$ -derived  $r_{200}$  cut (Column 10), dynamical complexity within a  $\sigma$ -derived  $r_{200}$  (Column 11); the number of member galaxies within an X-ray-derived  $r_{200}$  (Column 12); the radius in arcseconds of an X-ray-derived  $r_{200}$  (Column 13); velocity dispersion within an X-ray-derived  $r_{200}$  (Column 14); spectroscopic completeness (to  $R < 22$ ) within an X-ray-derived  $r_{200}$  cut (Column 15), and the dynamical complexity within an X-ray-derived  $r_{200}$  cut (Column 16).

**Table 5**  
Basic Properties of Optically Selected Groups

OID	R.A. (J2000)	Decl. (J2000)	$z$	XID	X-Ray Flux ( $10^{-14}$ erg cm $^{-2}$ s $^{-1}$ )	X-Ray Significance
OP14h01	222.42588	+9.05001	0.1648	XR14h12	$0.53 \pm 0.15$	3.45
OP14h08	222.24931	+9.16426	0.2287	...	<0.18	-1.5
OP14h09	222.22414	+8.94529	0.2616	...	<0.11	1.25
OP14h10	222.38704	+8.89722	0.2709	XR14h22 <sup>a</sup>	<0.10	-0.53
OP14h11	222.28817	+8.83040	0.2710	XR14h25 <sup>a</sup>	<0.11	1.39
OP14h15	222.19998	+8.96308	0.3070	...	<0.13	0.38
OP14h16	222.59024	+9.10364	0.3065	...	<0.31	0.87
OP14h19	222.55307	+8.96008	0.3251	...	<0.18	-0.54
OP14h24	222.26426	+9.11689	0.3593	...	<0.12	0.19
OP14h25	222.43995	+9.22828	0.3619	XR14h29 <sup>a</sup>	<2.72	-0.13
OP14h27	222.42101	+9.03718	0.3729	...	<0.19	1.95
OP14h28	222.59535	+9.01885	0.3729	XR14h18 <sup>a</sup>	<0.14	1.43
OP14h29	222.44650	+8.85237	0.3737	...	<0.12	-0.58
OP14h30	222.49989	+8.82020	0.3941	...	<0.13	1.53
OP14h31	222.31070	+9.18861	0.3934	...	$0.16 \pm 0.07$	2.11
OP14h32	222.48710	+8.92912	0.3948	...	<0.10	-0.84
OP14h34	222.16981	+8.85406	0.4658	...	<1.89	-0.06
OP14h37	222.38534	+9.07346	0.4717	XR14h11 <sup>a</sup>	<0.08	-0.12
OP14h36	222.37571	+9.15315	0.4693	...	<0.11	0.69
OP14h38	222.34864	+8.98095	0.5104	...	$0.10 \pm 0.04$	2.59
OP14h40	222.34715	+8.92136	0.5424	...	<0.06	-0.54
OP21h101	327.75074	-5.77684	0.1220	...	$0.28 \pm 0.13$	2.15
OP21h102	327.66348	-5.76956	0.1446	...	$0.31 \pm 0.11$	2.78
OP21h104	327.85585	-5.45052	0.1454	XR21h07	$3.91 \pm 0.18$	20.91
OP21h111	327.87688	-5.83900	0.1790	...	<2.44	-0.75
OP21h113	327.79113	-5.29070	0.1998	...	$0.70 \pm 0.21$	3.34
OP21h117	327.90130	-5.51873	0.2193	XR21h09	$0.21 \pm 0.06$	3.18
OP21h119	327.70455	-5.86617	0.2365	...	<0.14	1.33
OP21h120	328.04147	-5.58994	0.2414	...	<0.41	-0.56
OP21h123	327.70645	-5.79192	0.2641	...	<0.10	0.93
OP21h129	327.73460	-5.67694	0.3171	...	<0.07	0.27
OP21h132	327.66658	-5.67135	0.3596	...	$0.36 \pm 0.04$	7.61
OP21h133	327.70045	-5.63780	0.3733	...	<0.06	-0.97
OP21h134	327.63220	-5.70360	0.3918	...	<0.04	1.34
OP21h137	327.65508	-5.49026	0.4258	...	$0.10 \pm 0.05$	2.04
OP21h138	327.67050	-5.68197	0.4378	XR21h14	$1.17 \pm 0.08$	13.32
OP21h139	327.58913	-5.84084	0.4403	...	$0.25 \pm 0.11$	2.25
OP21h140	327.67658	-5.47646	0.4658	...	<0.07	0.02

**Notes.** Column description: group identification number for the optical system (Column 1); R.A. and decl. of the center of the extended X-ray emission for equinox J2000.0 (Column 2 and 3); spectroscopic redshift (Column 4); X-ray group ID where there is a confident match (Column 5); the total flux in the 0.5–2 keV band (Column 6); and significance of the X-ray flux (Column 7).

<sup>a</sup> Match to X-ray system but low X-ray significance using the optical center and aperture.

adjacent systems while still obtaining stable membership solutions, we tighten it from the value of five used in Wilman et al. (2005a), choosing instead the aspect ratio of 10. This aspect ratio is applied to all systems, including those that are optically selected.

In order to obtain an accurate estimate for groups which have relatively few members, the galaxies within this radius are ordered sequentially by redshift and the observed velocity dispersion,  $\sigma(v)_{\text{obs}}$ , is then calculated using the Gapper algorithm (Beers et al. 1990; Equation (3)) as follows:

$$\sigma(v)_{\text{obs}} = 1.135c \left( \frac{\sqrt{\pi}}{n(n-1)} \sum_{i=1}^{n-1} w_i g_i \right), \quad (3)$$

where  $w_i = i(n-1)$  and  $g_i = z_{i+1} - z_i$  and the 1.135 multiplicative factor corrects for the  $2\sigma$  clipping of a Gaussian velocity distribution.

This value is then shifted to a rest-frame velocity dispersion and, finally, the intrinsic velocity dispersion  $\sigma_{\text{intr}}$  is calculated by subtracting the errors from the redshift measurements in quadrature. The mean redshift of the members and new velocity dispersion is then used to recompute the redshift and spatial offsets and the entire process is repeated until a stable membership solution is attained. In cases where combined errors from the redshifts measurements are larger than the rest-frame velocity dispersion of the group, we place a  $1\sigma$  upper limit on the intrinsic velocity dispersion using Monte Carlo simulations. For all other groups, errors on the group velocity dispersion are calculated using the Jackknife technique (Efron 1982). Note that the assumption of symmetric errors in this case can result in an error measurement larger than the velocity dispersion itself. Figure 3 shows the velocity dispersions for all systems as a function of redshift.

In the rare cases where the algorithm oscillates infinitely between two membership solutions, we choose the solution with

**Table 6**  
Measured Properties of Optically Selected Groups

OID	$N$ 1 Mpc	Radius (")	$\sigma$ (km s <sup>-1</sup> )	Completeness $R < 22$	Dynamical Complexity	$N$ $r_{200,\sigma}$	Radius (")	$\sigma$ (km s <sup>-1</sup> )	Completeness $R < 22$	Dynamical Complexity	$N$ $r_{200,X}$	Radius (")	$\sigma$ (km s <sup>-1</sup> )	Completeness $R < 22$	Dynamical Complexity	
OP14h01	9	378.08	191 ± 88	0.70	...	6	159.41	197 ± 131	0.72	...	7	165.96	174 ± 112	0.72	...	
OP14h08	8	292.19	159 ± 101	0.59	...	4	123.00	204 ± 166	0.65	...	≤4	<115.92	204 ± 166	0.60	...	
OP14h09	10	264.17	168 ± 55	0.58	...	8	107.71	201 ± 56	0.40	...	≤8	<100.08	201 ± 56	0.43	...	
OP14h10	16	257.58	367 ± 59	0.72	DS	11	152.08	293 ± 68	0.83	...	≤7	<97.56	207 ± 72	0.93	...	
OP14h11	18	257.66	254 ± 42	0.54	...	15	134.54	259 ± 50	0.75	...	≤11	<98.64	274 ± 69	0.69	...	
OP14h15	7	235.96	110 ± 88	0.48	...	6	39.56	84 ± 110	0.70	...	≤7	<96.84	110 ± 88	0.65	...	
OP14h16	6	236.32	219 ± 73	0.53	...	5	89.54	192 ± 158	0.73	...	≤5	<114.84	192 ± 158	0.75	...	
OP14h19	7	227.06	174 ± 69	0.61	...	5	69.16	156 ± 182	0.47	...	≤5	<101.16	156 ± 182	0.48	...	
OP14h24	16	212.56	78 ± 41	0.74	AD	0	...	...	...	...	≤14	<89.64	87 ± 43	0.94	AD	
OP14h25	21	211.55	501 ± 78	0.65	...	21	202.95	501 ± 78	0.66	...	≤17	<171.00	447 ± 79	0.72	...	
OP14h27	4	207.70	129 ± 149	0.70	...	3	77.43	<196	0.92	...	≤3	<97.92	<193	0.80	...	
OP14h28	8	207.69	190 ± 62	0.54	...	4	49.79	126 ± 144	0.89	...	≤6	<91.80	174 ± 76	0.79	...	
OP14h29	8	207.22	297 ± 137	0.61	...	5	156.52	397 ± 205	0.71	...	≤4	<89.28	453 ± 313	0.83	...	
OP14h30	12	200.72	261 ± 80	0.36	...	6	95.45	253 ± 222	0.52	...	≤6	<88.56	253 ± 222	0.57	...	
OP14h31	7	200.86	304 ± 211	0.52	...	5	156.57	415 ± 252	0.62	...	5	92.16	415 ± 252	0.85	...	
OP14h32	10	200.80	910 ± 202	0.74	...	17	254.65	676 ± 150	0.73	DS	≤7	<83.88	822 ± 108	0.86	...	
OP14h34	6	181.92	139 ± 31	0.67	...	4	45.77	139 ± 170	0.86	...	≤6	<144.72	139 ± 31	0.79	...	
OP14h37	20	180.68	328 ± 46	0.77	DS	13	106.66	328 ± 64	0.83	AD	≤13	<75.96	414 ± 98	0.95	...	
OP14h36	6	181.16	183 ± 202	0.70	...	5	73.82	226 ± 247	0.73	...	≤6	<81.36	183 ± 202	0.67	...	
OP14h38	22	173.19	737 ± 57	0.76	AD	26	228.15	751 ± 52	0.74	AD	AD	10	78.12	673 ± 142	0.57	AD
OP14h40	3	167.84	213 ± 209	0.79	...	3	61.72	213 ± 209	1.00	...	≤3	<69.48	213 ± 209	0.88	...	
OP21h101	7	487.09	156 ± 69	0.56	...	0	...	...	...	...	3	169.92	112 ± 163	0.50	...	
OP21h102	12	421.00	148 ± 37	0.58	...	5	105.69	116 ± 61	0.50	...	6	159.48	117 ± 49	0.58	...	
OP21h104	46	419.27	443 ± 47	0.40	...	46	400.49	443 ± 47	0.41	...	36	267.12	485 ± 53	0.50	...	
OP21h111	10	353.44	371 ± 115	0.40	...	10	278.07	371 ± 115	0.37	...	≤6	<220.32	505 ± 192	0.38	...	
OP21h113	3	323.99	748 ± 558	0.29	...	6	334.91	494 ± 192	0.28	...	1	161.64	...	...	...	
OP21h117	29	300.99	259 ± 35	0.49	...	10	102.92	165 ± 34	0.68	...	10	121.68	165 ± 34	0.67	...	
OP21h119	4	284.51	122 ± 146	0.32	...	3	98.99	169 ± 139	0.61	...	≤3	<109.80	169 ± 139	0.55	...	
OP21h120	7	280.58	212 ± 77	0.26	...	5	94.51	164 ± 50	0.30	...	≤5	<133.92	164 ± 50	0.24	...	
OP21h123	13	262.25	194 ± 43	0.48	DS	6	88.39	166 ± 94	0.59	...	≤6	<99.00	166 ± 94	0.55	...	
OP21h129	10	230.80	207 ± 85	0.66	AD	10	94.05	207 ± 85	0.79	AD	≤10	<86.40	207 ± 85	0.81	AD	
OP21h132	7	212.44	413 ± 52	0.70	...	6	167.82	412 ± 126	0.71	...	4	112.32	491 ± 16	0.70	...	
OP21h133	4	207.40	204 ± 39	0.64	...	3	88.04	223 ± 277	0.53	...	≤3	<79.20	223 ± 277	0.56	...	
OP21h134	14	201.33	316 ± 67	0.70	...	12	129.98	343 ± 73	0.80	...	≤8	<72.00	385 ± 101	0.94	...	
OP21h137	11	191.50	374 ± 82	0.63	...	8	130.14	368 ± 128	0.71	...	7	82.08	302 ± 128	0.77	...	
OP21h138	45	188.41	724 ± 67	0.69	AD	59	236.16	684 ± 59	0.70	AD	33	134.28	697 ± 87	0.67	...	
OP21h139	16	187.79	237 ± 40	0.57	AD	9	83.64	243 ± 50	0.67	...	10	97.56	273 ± 54	0.69	...	
OP21h140	5	181.91	108 ± 82	0.61	...	3	60.38	184 ± 187	0.84	...	≤4	<74.88	144 ± 81	0.76	...	

**Notes.** Column description: group identification number for the optical system (Column 1); number of member galaxies within 1 Mpc (Column 2); the radius in arcseconds of 1 Mpc (Column 3); the velocity dispersion within a 1 Mpc cut (Column 4); spectroscopic completeness (to  $R < 22$ ) within a 1 Mpc cut (Column 5), dynamical complexity within a 1 Mpc cut (Column 6); the number of member galaxies within a  $\sigma$ -derived  $r_{200}$  (Column 7); the radius in arcseconds of a  $\sigma$ -derived  $r_{200}$  (Column 8); the velocity dispersion within a  $\sigma$ -derived  $r_{200}$  (Column 9); spectroscopic completeness (to  $R < 22$ ) within a  $\sigma$ -derived  $r_{200}$  cut (Column 10), dynamical complexity within a  $\sigma$ -derived  $r_{200}$  (Column 11); the number of member galaxies within an X-ray-derived  $r_{200}$  (Column 12); the radius in arcseconds of an X-ray-derived  $r_{200}$  (Column 13); velocity dispersion within an X-ray-derived  $r_{200}$  (Column 14); spectroscopic completeness (to  $R < 22$ ) within an X-ray-derived  $r_{200}$  cut (Column 15), and the dynamical complexity within an X-ray-derived  $r_{200}$  cut (Column 16).

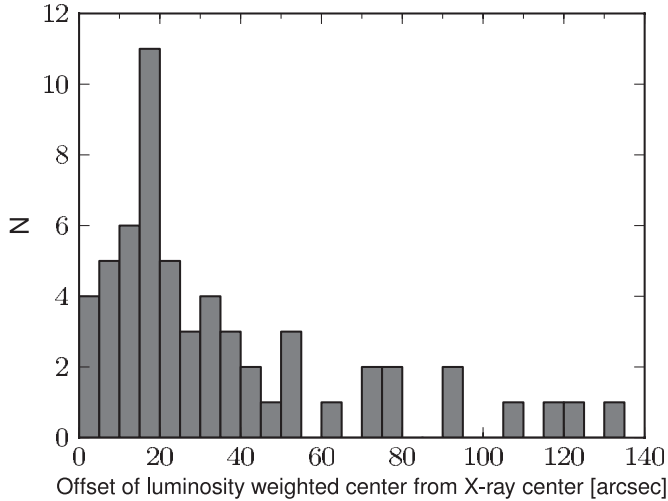


**Figure 4.** Histogram of offset between X-ray and luminosity-weighted centers for all X-ray systems having significance  $\geq 1$  without a radial cut applied.

more members. Note that in such cases it is possible that a few member galaxies lay outside the final quoted  $\delta(\theta)_{\max}$  since this quantity is calculated from the final velocity dispersion of the group. To evaluate the results of the membership assignment, especially in cases with more than one possible group redshift, we examine both the imaging (X-ray and optical) and velocity distribution of the group members.

#### 6.4. Group Centers

The process of assigning group membership is applied to both the X-ray and optically selected groups, using previously defined optical group centers for the latter. It is run twice, allowing for *R*-band luminosity-weighted recentering of the group in the second instance. In Figure 4, we compare the X-ray and luminosity-weighted centers for our X-ray groups. For the majority of systems, the center shifts  $\leq 18''$  when luminosity recentering is applied. Group membership and overall properties change very little using the luminosity-weighted center (see, e.g., Section 9) and we choose to adopt the X-ray centers for these systems in all subsequent analysis.

#### 6.5. Radial Cuts

Once the best redshift and membership is determined, we apply three different radial cuts to our groups: a constant cut of 1 Mpc and two  $r_{200}$  cuts defining the radius at which the density of the system is 200 times the critical density. Using the velocity dispersion ( $\sigma_{\text{intr}}$ ) and the definition of  $r_{200}$  as in Carlberg et al. (1997), we define a velocity dispersion based  $r_{200}$  as follows:

$$r_{200,\sigma} = \frac{\sigma_{\text{intr}}\sqrt{3}}{10H(z)}. \quad (4)$$

The second  $r_{200}$  cut is X-ray based and is discussed in Section 3. Using each of these radial cuts, the membership is redefined and a final  $\sigma$  computed. In the case of a velocity dispersion based  $r_{200}$ , the algorithm is allowed to iterate until a stable solution is found. Although these cuts often result in decreased membership, if the radial cut is larger than  $\delta(\theta)_{\max}$ , as is often the case for the 1 Mpc cut, the membership of the group may increase.

For those groups that are adjacent both in position on the sky and in redshift space (e.g., XR21h06 and XR21h07), members

may be shared across groups. As the original membership algorithm does *not* allow members to be in multiple groups and instead will merge such systems, discarding one group entirely, the discarded system in these adjacent groups will also have zero members given an  $r_{200,\sigma}$  radial cut. Distinct groups may also be entirely stripped of members given an  $r_{200,\sigma}$  if the initial velocity dispersion and subsequent iteration sufficiently reduces the redshift and spatial limits. This happens most commonly when group members are rather dispersed in projected position and have very similar velocities, causing the computed  $\sigma$  and  $r_{200,\sigma}$  to be low and many, or all, of these members to be discarded.

As group membership can change significantly given different definitions of group radius, the mean redshift of members may also change. For the vast majority of systems, the redshift varies little, being stable at least to the third decimal place, and approaches  $\sim 0.003$  only in the most extreme case. As the redshift of the group does not affect most quantities subsequently derived for the group, and those that are redshift dependent are not significantly affected by differences at the level observed, we choose to apply a single redshift in all cases. X-ray properties (i.e., luminosity and mass) were calculated using the redshift of the group derived with the initial cut, as defined by Equation (2), and this redshift is typically in very good agreement with those from the three radial cuts.

## 7. GROUP MASS ESTIMATES

Table 7 includes all three mass estimates (X-ray, dynamical, and stellar) for our X-ray-selected systems, listing the group identification number for the X-ray system (Column 1); rest-frame luminosity in the 0.1–2.4 keV band (Column 2); estimates of a total mass, using X-ray luminosity as a mass proxy and a calibration of Leauthaud et al. (2010) (Column 3); group stellar mass calculated using 1 Mpc,  $r_{200,\sigma}$ , and  $r_{200,X}$  radial cuts (Columns 4–6); and the dynamical (virial) mass for 1 Mpc,  $r_{200,\sigma}$ , and  $r_{200,X}$  radial cuts (Columns 7–9). Table 8 lists similar quantities for optically selected systems. In cases where there is no significant X-ray detection, we use the upper limit on  $r_{200,X}$  in our mass estimates. Stellar masses are then less than or equal to the derived measurement. Dynamical masses however may be accurate but could also be under or overestimates as lesser radius could act to increase or decrease  $\sigma$  in this case.

### 7.1. Dynamical Mass

We estimate dynamical masses,  $M_{\text{dynamical}}$  or  $M_{\text{dyn}}$ , for our groups from the velocity dispersion and radius as in Balogh et al. (2006) and Carlberg et al. (1999):

$$M_{\text{dyn}} = 3\sigma^2 r_{200}/G. \quad (5)$$

Note that the factor of three in this equation reflects the assumption of isotropic orbits and an isothermal potential, but is only weakly dependent on those assumptions (Łokas & Mamon 2001). We calculate dynamical masses for groups having a minimum of three members. In cases where the velocity dispersion is an upper limit, dynamical masses are also treated as upper limits. When calculating errors in dynamical mass, no estimation of error in  $r_{200}$  is included. Large errors in velocity dispersion, which may result from the assumption of symmetric errors made via the Jackknife technique, can result in dynamical mass errors larger than the measure itself.

**Table 7**  
Masses of X-Ray-selected Groups

XID	$L_X$ ( $10^{42}$ erg $s^{-1}$ )	$M_X$ ( $10^{13} M_\odot$ )	$M_{\text{stellar}}(1 \text{ Mpc})$ ( $10^{11} M_\odot$ )	$M_{\text{stellar}}(r_{200,\sigma})$ ( $10^{11} M_\odot$ )	$M_{\text{stellar}}(r_{200,X})$ ( $10^{11} M_\odot$ )	$M_{\text{dyn}}(1 \text{ Mpc})$ ( $10^{13} M_\odot$ )	$M_{\text{dyn}}(r_{200,\sigma})$ ( $10^{13} M_\odot$ )	$M_{\text{dyn}}(r_{200,X})$ ( $10^{13} M_\odot$ )
XR14h02	0.62 ± 0.22	1.38 ± 0.29	1.04 <sup>±0.55</sup> <sub>0.48</sub>	0.87 <sup>±0.49</sup> <sub>0.49</sub>	0.89 <sup>±0.49</sup> <sub>0.48</sub>	3.170 ± 1.001	0.700 ± 0.492	0.869 ± 0.612
XR14h09	34.6 ± 3.55	11.8 ± 0.76	>21.5	>30.6	>20.3	50.50 ± 13.36	54.09 ± 12.25	35.38 ± 12.28
XR14h10	6.55 ± 2.64	3.74 ± 0.90	>4.69	>4.76	>1.31	14.68 ± 11.80	10.32 ± 8.297	8.135 ± 10.37
XR21h08	2.54 ± 0.32	3.07 ± 0.24	2.87 <sup>±0.78</sup> <sub>0.71</sub>	2.27 <sup>±0.60</sup> <sub>0.56</sub>	2.54 <sup>±0.63</sup> <sub>0.54</sub>	4.815 ± 1.415	2.286 ± 0.992	3.078 ± 1.017
XR21h10	1.12 ± 0.34	1.72 ± 0.32	6.23 <sup>±3.73</sup> <sub>3.46</sub>	4.14 <sup>±2.88</sup> <sub>2.87</sub>	4.14 <sup>±2.88</sup> <sub>2.88</sub>	4.052 ± 1.205	0.602 ± 1.395	0.846 ± 1.963
XR21h11	2.98 ± 0.66	2.85 ± 0.39	11.2 <sup>±2.97</sup> <sub>2.52</sub>	10.1 <sup>±2.47</sup> <sub>2.01</sub>	9.51 <sup>±2.00</sup> <sub>1.83</sub>	9.766 ± 3.945	8.949 ± 3.737	6.474 ± 2.641
XR21h12	0.59 ± 0.18	1.24 ± 0.23	5.31 <sup>±0.89</sup> <sub>0.84</sub>	1.06 <sup>±0.21</sup> <sub>0.20</sub>	1.08 <sup>±0.19</sup> <sub>0.20</sub>	4.570 ± 1.144	2.705 ± 1.601	2.071 ± 1.226
XR21h14	26.1 ± 0.99	11.8 ± 0.28	12.2 <sup>±1.93</sup> <sub>1.80</sub>	21.2 <sup>±3.61</sup> <sub>3.16</sub>	8.20 <sup>±1.97</sup> <sub>1.74</sub>	39.24 ± 7.647	40.77 ± 7.241	28.41 ± 6.542
XR21h15	6.77 ± 2.52	3.84 ± 0.86	>11.5	>12.9	>14.5	10.21 ± 15.46	6.008 ± 9.090	5.154 ± 7.797
XR21h60	1.44 ± 0.34	2.05 ± 0.30	2.48 <sup>±1.99</sup> <sub>1.97</sub>	...	2.51 <sup>±1.91</sup> <sub>1.91</sub>	<1.708	...	0.385 ± 0.929
XR21h64	1.99 ± 0.38	2.65 ± 0.31	1.67 <sup>±0.74</sup> <sub>0.60</sub>	1.47 <sup>±0.38</sup> <sub>0.46</sub>	1.44 <sup>±0.40</sup> <sub>0.44</sub>	2.243 ± 1.319	1.847 ± 4.482	2.061 ± 5.003
XR21h09	1.33 ± 0.17	2.10 ± 0.17	6.83 <sup>±1.62</sup> <sub>1.18</sub>	2.62 <sup>±1.23</sup> <sub>1.01</sub>	3.17 <sup>±1.13</sup> <sub>1.05</sub>	4.574 ± 1.306	0.649 ± 0.267	1.588 ± 0.623
XR14h03	11.2 ± 3.17	5.04 ± 0.87	>9.30	>9.34	>7.00	51.58 ± 25.65	48.67 ± 26.94	30.53 ± 39.05
XR14h08	6.95 ± 1.64	4.77 ± 0.69	1.68 <sup>±0.43</sup> <sub>0.27</sub>	...	1.87 <sup>±0.39</sup> <sub>0.34</sub>	0.759 ± 1.843	<0.133	0.399 ± 1.083
XR14h18	3.04 ± 1.01	3.15 ± 0.63	3.51 <sup>±1.10</sup> <sub>0.90</sub>	1.82 <sup>±0.56</sup> <sub>0.58</sub>	3.02 <sup>±0.81</sup> <sub>0.83</sub>	1.597 ± 1.542	0.266 ± 0.608	1.154 ± 1.006
XR14h22	0.60 ± 0.28	1.22 ± 0.34	4.41 <sup>±1.39</sup> <sub>1.13</sub>	2.39 <sup>±1.21</sup> <sub>1.20</sub>	2.28 <sup>±1.02</sup> <sub>0.98</sub>	10.19 ± 2.290	3.529 ± 1.854	1.554 ± 1.029
XR14h25	1.30 ± 0.36	1.99 ± 0.34	4.50 <sup>±0.84</sup> <sub>0.83</sub>	1.99 <sup>±0.43</sup> <sub>0.35</sub>	1.79 <sup>±0.40</sup> <sub>0.33</sub>	4.998 ± 1.622	2.858 ± 1.186	2.737 ± 1.292
XR14h35	6.05 ± 1.87	3.88 ± 0.73	>1.83	>0.94	>0.94	21.65 ± 11.95	13.03 ± 24.34	8.652 ± 16.16
XR14h40	5.03 ± 3.04	3.46 ± 1.22	>2.26	>2.05	>2.73	<6.265	<3.025	<3.007
XR14h44	3.96 ± 1.52	3.04 ± 0.70	>13.2	>13.2	>4.41	25.09 ± 7.646	24.88 ± 7.580	5.770 ± 11.45
XR21h06	1.08 ± 0.15	1.94 ± 0.17	7.38 <sup>±2.31</sup> <sub>1.63</sub>	6.13 <sup>±1.86</sup> <sub>1.53</sub>	2.54 <sup>±0.77</sup> <sub>0.69</sub>	12.66 ± 2.755	12.11 ± 2.598	3.893 ± 1.559
XR21h07	7.17 ± 0.15	6.51 ± 0.09	6.85 <sup>±2.33</sup> <sub>1.74</sub>	...	5.65 <sup>±1.74</sup> <sub>1.38</sub>	13.73 ± 2.954	...	11.70 ± 2.439
XR21h13	0.36 ± 0.24	0.89 ± 0.34	0.21 <sup>±0.05</sup> <sub>0.06</sub>	0.17 <sup>±0.05</sup> <sub>0.05</sub>	0.17 <sup>±0.05</sup> <sub>0.04</sub>	<0.697	<0.142	<0.259
XR21h18	1.17 ± 0.44	1.69 ± 0.38	2.76 <sup>±1.15</sup> <sub>1.05</sub>	...	1.92 <sup>±0.56</sup> <sub>0.57</sub>	4.175 ± 1.816	...	1.440 ± 0.763
XR21h20	<0.37	<0.98	0.41 <sup>±0.14</sup> <sub>0.12</sub>	0.39 <sup>±0.14</sup> <sub>0.10</sub>	≤0.24 <sup>±0.12</sup> <sub>0.10</sub>	9.142 ± 3.535	6.065 ± 2.826	0.749 ± 1.085
XR21h23	5.59 ± 1.45	4.60 ± 0.73	0.42 <sup>±0.09</sup> <sub>0.08</sub>	...	0.40 <sup>±0.08</sup> <sub>0.08</sub>	15.22 ± 35.19	...	<0.425
XR21h31	1.03 ± 0.92	1.46 ± 0.74	6.25 <sup>±1.33</sup> <sub>1.15</sub>	1.50 <sup>±0.96</sup> <sub>1.10</sub>	3.48 <sup>±0.85</sup> <sub>0.92</sub>	1.135 ± 0.588	0.161 ± 0.361	0.124 ± 0.376
XR21h32	7.51 ± 1.58	4.10 ± 0.53	...	...	...	<1.342	...	<1.773
XR21h33	1.71 ± 0.78	2.15 ± 0.58	1.23 <sup>±0.35</sup> <sub>0.29</sub>	0.39 <sup>±0.09</sup> <sub>0.11</sub>	1.14 <sup>±0.34</sup> <sub>0.29</sub>	2.734 ± 1.618	1.343 ± 0.711	1.558 ± 0.825
XR21h37	1.92 ± 0.54	2.22 ± 0.38	9.38 <sup>±1.61</sup> <sub>1.59</sub>	19.0 <sup>±3.26</sup> <sub>2.67</sub>	6.33 <sup>±1.21</sup> <sub>1.19</sub>	52.11 ± 11.40	94.98 ± 19.23	27.74 ± 7.140
XR21h42	0.76 ± 0.38	1.27 ± 0.38	1.53 <sup>±0.51</sup> <sub>0.50</sub>	0.82 <sup>±0.46</sup> <sub>0.48</sub>	1.51 <sup>±0.70</sup> <sub>0.95</sub>	0.752 ± 0.895	0.178 ± 0.387	0.339 ± 0.739
XR21h50	4.12 ± 1.88	3.24 ± 0.88	3.25 <sup>±2.61</sup> <sub>0.22</sub>	...	3.20 <sup>±0.74</sup> <sub>0.44</sub>	15.41 ± 12.64	...	1.440 ± 3.186
XR21h55	1.00 ± 0.20	1.70 ± 0.21	1.61 <sup>±0.47</sup> <sub>0.39</sub>	1.34 <sup>±0.43</sup> <sub>0.37</sub>	0.97 <sup>±0.44</sup> <sub>0.37</sub>	8.056 ± 3.856	5.543 ± 3.299	4.947 ± 3.716
XR14h11	2.38 ± 0.68	2.48 ± 0.43	18.1 <sup>±3.07</sup> <sub>3.17</sub>	4.69 <sup>±0.91</sup> <sub>0.92</sub>	4.55 <sup>±0.99</sup> <sub>0.99</sub>	7.641 ± 2.544	1.350 ± 0.863	1.644 ± 1.050
XR14h12	0.84 ± 0.20	1.64 ± 0.23	0.87 <sup>±0.42</sup> <sub>0.32</sub>	0.50 <sup>±0.27</sup> <sub>0.26</sub>	0.52 <sup>±0.29</sup> <sub>0.25</sub>	2.565 ± 2.375	0.754 ± 1.651	1.283 ± 1.704
XR14h19	11.6 ± 1.71	5.92 ± 0.54	...	...	...	...	...	...
XR14h29	3.58 ± 0.80	3.53 ± 0.48	8.05 <sup>±3.53</sup> <sub>3.16</sub>	7.28 <sup>±3.61</sup> <sub>3.21</sub>	2.13 <sup>±0.62</sup> <sub>0.53</sub>	12.79 ± 4.102	10.01 ± 3.505	9.698 ± 4.409
XR14h33	<19.2	<6.98	>0.85	>0.85	≈ 0.85	8.839 ± 15.82	4.610 ± 8.251	5.252 ± 9.400
XR21h27	0.90 ± 0.18	1.69 ± 0.21	...	2.13 <sup>±0.53</sup> <sub>0.53</sub>	...	100.3 ± 47.22	798.4 ± 131.1	16.23 ± 10.23
XR14h01	7.73 ± 1.06	5.72 ± 0.49	19.7 <sup>±9.12</sup> <sub>7.79</sub>	...	52.6 <sup>±23.2</sup> <sub>23.8</sub>	<0.836	...	<1.003
XR14h05	8.36 ± 2.85	4.18 ± 0.86	...	...	...	23.04 ± 28.81	19.71 ± 24.64	...
XR14h07	9.89 ± 2.95	5.75 ± 1.04	...	...	...	...	...	...
XR14h13	4.78 ± 1.61	3.59 ± 0.73	...	...	...	...	...	...
XR14h23	60.1 ± 4.75	14.2 ± 0.71	...	...	...	27.87 ± 7.123	25.57 ± 6.534	20.94 ± 5.352
XR14h24	19.7 ± 5.00	5.93 ± 0.92	...	...	...	...	...	...
XR14h26	9.97 ± 4.82	4.71 ± 1.35	>2.78	...	>0.59	2.953 ± 2.703	...	0.624 ± 1.568
XR14h37	<5.19	<3.79	20.4 <sup>±8.40</sup> <sub>4.78</sub>	...	≤5.84 <sup>±2.34</sup> <sub>1.43</sub>	14.85 ± 10.91	...	3.268 ± 7.797
XR14h38	<2.71	<3.12	...	...	...	...	...	...
XR14h39	0.80 ± 0.73	1.47 ± 0.75	...	...	...	...	...	...
XR14h41	7.33 ± 2.90	3.49 ± 0.83	...	...	...	...	...	...
XR14h47	2.94 ± 0.84	3.00 ± 0.52	...	...	...	...	...	...
XR21h16	1.05 ± 0.50	1.57 ± 0.45	3.64 <sup>±0.88</sup> <sub>0.89</sub>	...	...	6.751 ± 3.277	...	...
XR21h17	3.44 ± 3.01	2.38 ± 1.17	>17.6	...	>15.2	3.646 ± 5.069	...	0.163 ± 0.711

**Table 7**  
(Continued)

XID	$L_X$ ( $10^{42}$ erg s $^{-1}$ )	$M_X$ ( $10^{13} M_\odot$ )	$M_{\text{stellar}}(1 \text{ Mpc})$ ( $10^{11} M_\odot$ )	$M_{\text{stellar}}(r_{200,\sigma})$ ( $10^{11} M_\odot$ )	$M_{\text{stellar}}(r_{200,X})$ ( $10^{11} M_\odot$ )	$M_{\text{dyn}}(1 \text{ Mpc})$ ( $10^{13} M_\odot$ )	$M_{\text{dyn}}(r_{200,\sigma})$ ( $10^{13} M_\odot$ )	$M_{\text{dyn}}(r_{200,X})$ ( $10^{13} M_\odot$ )
XR21h19	<2.94	<2.61	$3.15^{+2.53}_{-0.21}$	...	$\leq 3.15^{+0.94}_{-0.21}$	$7.592 \pm 10.20$	...	$3.579 \pm 4.812$
XR21h21	$4.95 \pm 0.96$	$4.07 \pm 0.49$	$11.4^{+2.68}_{-2.16}$	$6.25^{+2.42}_{-2.17}$	$7.17^{+2.43}_{-2.19}$	$6.664 \pm 2.145$	$2.390 \pm 0.731$	$3.482 \pm 1.150$
XR21h30	<0.73	<1.24	$0.88^{+0.17}_{-0.14}$	$0.95^{+0.20}_{-0.20}$	...	$10.29 \pm 14.80$	$7.421 \pm 10.67$	...
XR21h40	$7.22 \pm 2.09$	$4.29 \pm 0.75$	...	...	...	...	...	...
XR21h41	<11.3	<4.72	...	...	...	...	...	...
XR21h43	$1.81 \pm 1.23$	$1.85 \pm 0.73$	>1.92	>2.13	>2.13	$5.349 \pm 6.855$	$2.457 \pm 3.148$	$1.233 \pm 2.988$
XR21h48	<0.58	<1.20	$0.39^{+0.13}_{-0.11}$	...	...	$1.772 \pm 2.669$	...	...
XR21h49	$0.84 \pm 0.57$	$1.35 \pm 0.53$	$6.58^{+1.92}_{-1.54}$	$11.7^{+1.88}_{-1.78}$	...	$38.73 \pm 14.68$	$85.07 \pm 19.50$	...
XR21h59	$3.10 \pm 0.72$	$3.01 \pm 0.43$	$4.74^{+0.85}_{-0.80}$	$6.49^{+1.08}_{-1.05}$	$2.42^{+0.32}_{-0.02}$	$33.15 \pm 13.15$	$48.68 \pm 18.00$	$23.26 \pm 21.52$
XR21h69	$13.5 \pm 2.95$	$6.31 \pm 0.85$	>2.52	>4.32	...	$63.25 \pm 66.19$	$95.97 \pm 31.57$	...
XR14h04	$1.50 \pm 0.31$	$2.28 \pm 0.29$	$0.46^{+0.16}_{-0.14}$	$0.34^{+0.12}_{-0.14}$	$0.34^{+0.12}_{-0.14}$	$1.704 \pm 1.072$	$0.232 \pm 0.524$	$0.492 \pm 1.113$
XR14h14	$12.4 \pm 2.39$	$5.74 \pm 0.68$	>6.70	>7.18	>2.61	$63.16 \pm 47.81$	$76.99 \pm 54.54$	$23.49 \pm 17.36$
XR21h22	$8.47 \pm 4.48$	$4.33 \pm 1.35$	...	...	...	...	...	...
XR21h67	$9.11 \pm 1.65$	$5.97 \pm 0.67$	$33.9^{+28.5}_{-28.5}$	...	$32.8^{+27.7}_{-27.5}$	$0.451 \pm 0.773$	...	$0.284 \pm 0.333$

**Notes.** Column description: group identification number for the X-ray system (Column 1); rest-frame luminosity in the 0.1–2.4 keV band (Column 2); estimates of a total mass, using X-ray luminosity as a mass proxy and a calibration of Leauthaud et al. (2010) (Column 3); group stellar mass calculated using 1 Mpc,  $r_{200,\sigma}$ , and  $r_{200,X}$  radial cuts (Columns 4–6); and the dynamical (virial) mass for 1 Mpc,  $r_{200,\sigma}$ , and  $r_{200,X}$  radial cuts (Columns 7–9).

### 7.2. X-Ray Mass

X-ray masses are estimated using the  $z \sim 0.25$  relation from Leauthaud et al. (2010). Standard evolution of the scaling relations,  $M_{200}E_z = f(L_X E_z^{-1})$  where  $E_z = (\Omega_M(1+z)^3 + \Omega_\Lambda)^{1/2}$ , is assumed and these relations verified using a weak-lensing calibration of X-ray groups in the COSMOS survey (Leauthaud et al. 2010). In order to use this calibration, a “concordance” cosmology with  $H_0 = 72 \text{ km s}^{-1} \text{ Mpc}^{-1}$ ,  $\Omega_M = 0.25$ , and  $\Omega_\Lambda = 0.75$  is applied. X-ray masses quoted for X-ray and optically selected groups with low (<1 and <2, respectively) X-ray significance are  $2\sigma$  upper limits.

### 7.3. Stellar Mass

In order to derive accurate total stellar masses for our groups, we must correct for incompleteness. The first major contribution to this incompleteness is the lack of spectra for *all* objects in our fields. To correct for this, we compute the fraction of objects with redshifts for each group within its radial cut as a function of  $R$ -band (used for spectroscopic selection) magnitude  $f_z(R)$ . We apply a small correction to this fraction to account for the fact that a small percentage of these objects are likely to be stars. This minor correction is itself a function of the  $R$ -band magnitude and star/galaxy classification. We then calculate the fraction of members, again as a function of  $R$ -band magnitude, by computing the number of known members and dividing this total by the fraction of galaxies having redshifts  $f_{\text{mem}}(R) = N_{\text{mem}}(R)/N_z(R)$ . Finally, the galaxy masses are weighted to correct for this incompleteness as a function of  $R$ -band magnitude:  $\text{weight}_{\text{mem}}(R, M_{\text{stellar}}) = 1 + (1 - f_z(R))/f_z(R) \times f_{\text{mem}}(R)$ .

The second major source of incompleteness results from the magnitude limit of our spectroscopy. We begin by recalling our overall  $R$ -band magnitude limit of 22. This limit means that low-mass, faint galaxies will be missed. The mass at fixed magnitude is a function of mass-to-light ( $M/L$ ) ratio. Therefore, in order to calculate the appropriate stellar mass limit for each group, we find the mass of a high  $M/L$  galaxy at the  $R = 22$

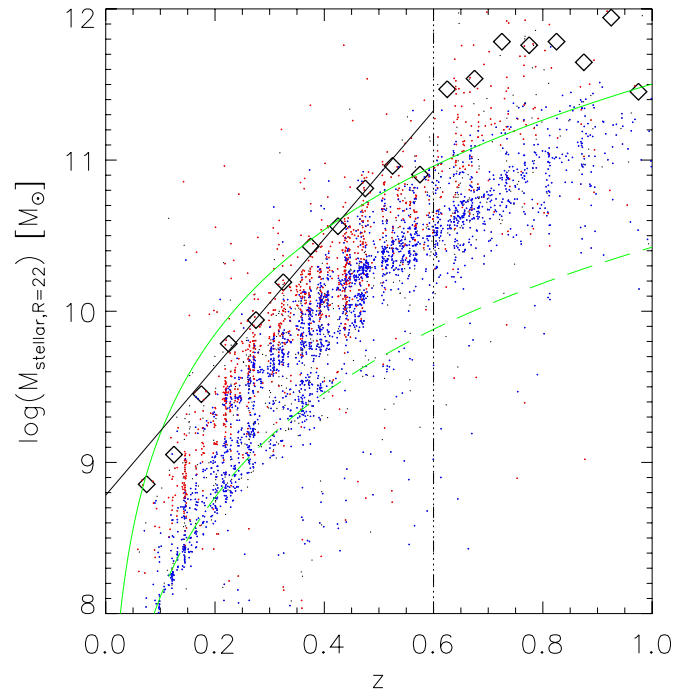


**Figure 5.** Stellar mass limit as a function of redshift. Red and blue dots, respectively, indicate red and blue galaxies, based on rest-frame  $U - R$  colors. Open black diamonds indicate the 90th percentile value of the mass estimates for a red galaxy with  $R = 22$ , and the black solid line is a simple fit to these points for  $z < 0.6$ . The vertical dot-dashed line indicates  $z = 0.6$ ; no further extrapolation to lower mass is performed at  $z > 0.6$ . Green solid and dashed lines represent an  $M/L$  ratio of 12 and 1, respectively.

(A color version of this figure is available in the online journal.)

magnitude limit as a function of redshift. Figure 5 shows the limit in stellar mass as a function of redshift. By examining the distribution of rest-frame  $U - R$  color as a function of redshift, we define a line separating the blue and red galaxy populations and categorize all galaxies with  $U - R > (0.2 \times z) - 1.5$  as red and the rest as blue. In a given redshift bin, we calculate the mass

**Table 8**  
Masses of Optically Selected Groups

OID	$L_X$ ( $10^{42}$ erg s $^{-1}$ )	$M_X$ ( $10^{13} M_\odot$ )	$M_{\text{stellar}}(1 \text{ Mpc})$ ( $10^{11} M_\odot$ )	$M_{\text{stellar}}(r_{200,\sigma})$ ( $10^{11} M_\odot$ )	$M_{\text{stellar}}(r_{200,X})$ ( $10^{11} M_\odot$ )	$M_{\text{dyn}}(1 \text{ Mpc})$ ( $10^{13} M_\odot$ )	$M_{\text{dyn}}(r_{200,\sigma})$ ( $10^{13} M_\odot$ )	$M_{\text{dyn}}(r_{200,X})$ ( $10^{13} M_\odot$ )
OP14h01	0.62 ± 0.18	1.34 ± 0.23	0.87 $^{+0.41}_{-0.33}$	0.52 $^{+0.28}_{-0.28}$	0.53 $^{+0.30}_{-0.27}$	2.565 ± 2.375	1.153 ± 1.530	0.928 ± 1.200
OP14h08	<0.46	<1.05	0.77 $^{+0.21}_{-0.19}$	0.46 $^{+0.13}_{-0.12}$	≤0.57 $^{+0.10}_{-0.10}$	1.781 ± 2.253	1.230 ± 2.007	1.159 ± 1.891
OP14h09	<0.40	<0.95	1.32 $^{+0.49}_{-0.46}$	1.37 $^{+0.45}_{-0.38}$	≤1.35 $^{+0.42}_{-0.39}$	1.983 ± 1.304	1.154 ± 0.641	1.073 ± 0.596
OP14h10	<0.42	<0.96	3.74 $^{+1.19}_{-1.08}$	2.90 $^{+1.16}_{-1.03}$	≤2.33 $^{+1.06}_{-1.15}$	9.425 ± 2.824	3.540 ± 1.652	1.142 ± 0.800
OP14h11	<0.44	<0.99	2.80 $^{+0.50}_{-0.41}$	2.24 $^{+0.41}_{-0.35}$	≤1.71 $^{+0.42}_{-0.35}$	4.509 ± 1.503	2.453 ± 0.952	2.011 ± 1.012
OP14h15	<0.67	<1.27	3.64 $^{+1.71}_{-1.49}$	1.40 $^{+0.34}_{-0.35}$	≤1.26 $^{+0.45}_{-0.36}$	0.859 ± 1.377	0.084 ± 0.219	0.352 ± 0.565
OP14h16	<1.50	<2.12	1.67 $^{+0.75}_{-0.59}$	1.44 $^{+0.64}_{-0.73}$	≤1.41 $^{+0.77}_{-0.72}$	3.367 ± 2.261	0.975 ± 1.605	1.250 ± 2.059
OP14h19	<1.04	<1.65	4.20 $^{+1.13}_{-1.11}$	3.15 $^{+0.51}_{-0.51}$	≤2.67 $^{+0.62}_{-0.64}$	2.124 ± 1.689	0.517 ± 1.213	0.756 ± 1.774
OP14h24	<0.90	<1.46	5.04 $^{+0.98}_{-1.18}$	...	≤3.69 $^{+1.05}_{-0.91}$	0.430 ± 0.451	...	0.225 ± 0.223
OP14h25	<19.2	<10.3	9.55 $^{+3.79}_{-3.02}$	9.52 $^{+4.03}_{-2.97}$	≤8.83 $^{+3.35}_{-8.83}$	17.54 ± 5.457	16.83 ± 5.235	11.30 ± 4.031
OP14h27	<1.57	<2.06	0.82 $^{+0.18}_{-0.20}$	0.62 $^{+0.13}_{-0.13}$	≤0.67 $^{+0.07}_{-0.10}$	1.160 ± 2.693	<1.001	<1.235
OP14h28	<1.17	<1.71	3.53 $^{+1.12}_{-0.99}$	1.33 $^{+0.41}_{-0.35}$	≤2.55 $^{+0.63}_{-0.64}$	2.536 ± 1.672	0.266 ± 0.608	0.943 ± 0.822
OP14h29	<1.04	<1.59	8.79 $^{+6.76}_{-6.01}$	1.63 $^{+0.45}_{-0.38}$	≤1.08 $^{+0.33}_{-0.28}$	6.160 ± 5.715	8.313 ± 8.600	6.175 ± 8.529
OP14h30	<1.24	<1.75	13.0 $^{+2.98}_{-2.72}$	11.7 $^{+3.16}_{-2.54}$	≤11.7 $^{+2.69}_{-2.59}$	4.763 ± 2.930	2.133 ± 3.747	1.978 ± 3.476
OP14h31	1.48 ± 0.70	1.95 ± 0.55	2.07 $^{+0.98}_{-0.89}$	1.63 $^{+0.87}_{-0.85}$	1.56 $^{+0.81}_{-0.80}$	6.456 ± 8.968	9.373 ± 11.38	5.517 ± 6.699
OP14h32	<0.96	<1.49	2.16 $^{+0.56}_{-0.53}$	2.77 $^{+0.63}_{-0.50}$	≤1.40 $^{+0.42}_{-0.42}$	57.79 ± 25.69	40.45 ± 18	19.71 ± 5.216
OP14h34	<24.5	<11.0	7.46 $^{+2.57}_{-2.38}$	6.50 $^{+2.73}_{-2.22}$	≤7.36 $^{+2.53}_{-2.27}$	1.359 ± 0.620	0.342 ± 0.836	1.081 ± 0.493
OP14h37	<1.27	<1.65	17.2 $^{+3.56}_{-3.22}$	14.3 $^{+2.70}_{-2.25}$	≤13.2 $^{+2.30}_{-2.25}$	7.527 ± 2.118	4.450 ± 1.753	5.027 ± 2.386
OP14h36	<1.70	<2.00	10.2 $^{+2.05}_{-2.53}$	11.3 $^{+1.60}_{-1.60}$	≤11.3 $^{+1.56}_{-1.57}$	2.336 ± 5.161	1.461 ± 3.192	1.049 ± 2.317
OP14h38	1.98 ± 0.76	2.13 ± 0.49	21.1 $^{+5.39}_{-4.00}$	36.7 $^{+13.1}_{-10.4}$	15.6 $^{+4.39}_{-3.66}$	37.93 ± 5.949	51.85 ± 7.179	14.26 ± 6.028
OP14h40	<1.48	<1.72	2.71 $^{+0.82}_{-0.40}$	3.78 $^{+1.39}_{-0.93}$	≤3.63 $^{+1.42}_{-0.79}$	3.185 ± 6.243	1.171 ± 2.296	1.318 ± 2.584
OP21h101	0.18 ± 0.08	0.64 ± 0.17	0.32 $^{+0.12}_{-0.13}$	...	0.23 $^{+0.07}_{-0.07}$	1.712 ± 1.527	...	0.306 ± 0.893
OP21h102	0.29 ± 0.10	0.84 ± 0.18	1.15 $^{+0.49}_{-0.42}$	0.95 $^{+0.37}_{-0.37}$	0.96 $^{+0.44}_{-0.96}$	1.548 ± 0.789	0.237 ± 0.251	0.362 ± 0.308
OP21h104	3.36 ± 0.16	4.01 ± 0.12	6.81 $^{+2.08}_{-1.62}$	6.86 $^{+2.16}_{-1.68}$	5.7 $^{+2.07}_{-5.7}$	13.73 ± 2.914	13.11 ± 2.822	10.48 ± 2.299
OP21h111	<3.32	<3.88	1.04 $^{+0.28}_{-0.28}$	0.80 $^{+0.28}_{-0.25}$	≤0.60 $^{+0.30}_{-0.24}$	9.646 ± 6.011	7.589 ± 4.729	11.08 ± 8.430
OP21h113	1.23 ± 0.37	2.03 ± 0.37	0.54 $^{+0.48}_{-0.49}$	0.54 $^{+0.50}_{-0.48}$	...	39.09 ± 58.35	17.61 ± 13.72	...
OP21h117	0.49 ± 0.15	1.10 ± 0.21	7.27 $^{+1.63}_{-1.36}$	2.96 $^{+1.18}_{-1.03}$	2.96 $^{+1.27}_{-2.96}$	4.692 ± 1.122	0.649 ± 0.267	0.767 ± 0.316
OP21h119	<0.41	<0.98	0.89 $^{+0.13}_{-0.11}$	0.87 $^{+0.11}_{-0.11}$	≤0.87 $^{+0.11}_{-0.11}$	1.054 ± 2.519	0.697 ± 1.146	0.773 ± 1.271
OP21h120	<1.15	<1.88	1.18 $^{+0.50}_{-0.43}$	1.26 $^{+0.35}_{-0.32}$	≤1.23 $^{+0.38}_{-0.29}$	3.146 ± 2.295	0.638 ± 0.391	0.905 ± 0.555
OP21h123	<0.40	<0.94	4.92 $^{+1.06}_{-0.92}$	3.04 $^{+0.47}_{-0.47}$	≤3.57 $^{+0.47}_{-0.47}$	2.642 ± 1.174	0.654 ± 0.738	0.732 ± 0.827
OP21h129	<0.45	<0.98	1.23 $^{+0.30}_{-0.25}$	2.08 $^{+0.66}_{-0.46}$	≤1.97 $^{+0.55}_{-0.44}$	3.008 ± 2.482	1.225 ± 1.011	1.126 ± 0.929
OP21h132	2.60 ± 0.34	2.88 ± 0.23	1.55 $^{+0.87}_{-0.81}$	1.32 $^{+0.89}_{-0.86}$	1.20 $^{+0.89}_{-0.89}$	11.92 ± 3.017	9.387 ± 5.761	8.900 ± 0.610
OP21h133	<0.59	<1.10	1.60 $^{+0.37}_{-0.35}$	1.49 $^{+0.35}_{-0.34}$	≤1.49 $^{+0.35}_{-0.36}$	2.919 ± 1.133	1.476 ± 3.667	1.327 ± 3.299
OP21h134	<0.46	<0.93	4.93 $^{+0.83}_{-0.86}$	4.21 $^{+0.78}_{-0.74}$	≤2.80 $^{+0.67}_{-0.65}$	7.005 ± 2.971	5.309 ± 2.274	3.712 ± 1.959
OP21h137	1.19 ± 0.58	1.65 ± 0.48	5.84 $^{+1.74}_{-1.40}$	4.66 $^{+1.55}_{-1.31}$	4.65 $^{+1.42}_{-1.32}$	9.771 ± 4.325	6.439 ± 4.481	2.728 ± 2.321
OP21h138	13.4 ± 1.00	7.72 ± 0.36	10.8 $^{+2.14}_{-1.67}$	21.2 $^{+3.63}_{-2.79}$	7.19 $^{+1.90}_{-1.71}$	36.63 ± 6.905	40.98 ± 7.105	24.20 ± 6.053
OP21h139	3.09 ± 1.37	3.01 ± 0.79	9.40 $^{+2.75}_{-2.29}$	7.43 $^{+2.10}_{-1.98}$	8.32 $^{+2.28}_{-1.91}$	3.923 ± 1.242	1.843 ± 0.756	2.701 ± 1.083
OP21h140	<1.12	<1.54	3.30 $^{+1.13}_{-0.85}$	2.74 $^{+0.64}_{-0.58}$	≤3.50 $^{+1.20}_{-0.97}$	0.815 ± 1.241	0.787 ± 1.596	0.597 ± 0.672

**Notes.** Column description: group identification number for the optical system (Column 1); rest-frame luminosity in the 0.1–2.4 keV band (Column 2); estimates of a total mass, using X-ray luminosity as a mass proxy and a calibration of Leauthaud et al. (2010) (Column 3); group stellar mass calculated using 1 Mpc,  $r_{200,\sigma}$ , and  $r_{200,X}$  radial cuts (Columns 4–6); and the dynamical (virial) mass for 1 Mpc,  $r_{200,\sigma}$ , and  $r_{200,X}$  radial cuts (Columns 7–9).

each galaxy would have if it were observed at the magnitude limit of  $R = 22$  and with its own mass-to-light ratio in that band:  $M_{\text{stellar},R=22}(z) = M_{\text{stellar}}(z) \times 10^{-0.4(22.-R(z))}$ . Finally, we compute the 90th percentile value of these mass estimates for the red galaxies in each redshift bin (these are the black diamonds in Figure 5) and perform a simple linear fit to these values to define  $M_{\text{stellar\_lim}}(z)$ , up to a maximum  $z = 0.6$  above which this completeness limit becomes unusefully high. This fit is comparable to what one would obtain from assuming a mass-to-light ratio of 12. Finally, we calculate a mass cutoff for each group,  $M_{\text{cut,group}}$  using its redshift.

In order to extrapolate the mass below the limit at which we are complete, we first take our lowest redshift groups and fit a Schechter function. Using the parameters from this local Schechter function fit, we then extrapolate the stellar mass of each group below  $M_{\text{cut,group}}$  down to a constant cutoff  $M_{\text{cut}} = 10^{10} M_\odot$ . We find that the parameters for a system with  $\log(M_{\text{halo}}) = 13.64$  from Yang et al. (2009), with  $\alpha = -1.22$  and  $\log(M_*) = 11.122$ , provide a reasonable fit for our local groups—these parameters are then used for the extrapolation. The final, corrected total group stellar mass is then summed down to our constant mass limit of  $10^{10} M_\odot$ . For groups at



redshifts  $z > 0.6$ , Schechter function based extrapolation is not used and instead the total measured stellar mass of known members is considered a lower limit. Note that we calculate stellar masses only for groups with three or more members.

To calculate errors on the stellar mass determinations for our groups we account for the sampling error by bootstrapping the membership allocation above the mass limit at the group redshift, allowing the galaxies to be selected more than once. We also resample the fraction of galaxies with known redshifts which are members  $f_{\text{mem}}(R)$  selecting from a binomial distribution. In cases where  $f_{\text{mem}} = 0$  or 1, we choose to binomially resample the fraction of members presuming that the true fraction is different from these extreme values by 0.5 times the resolution ( $\langle f_{\text{mem}} \rangle = 0.5/N_z(R)$  or  $1-0.5/N_z(R)$ ). For groups with  $z < 0.6$  where  $M_{\text{cut,group}} > 10^{10} M_{\odot}$ , the extrapolation to lower mass (below the group mass limit) introduces additional uncertainty via the choice of the Schechter function parameters. To quantify this, we resample the correction randomly from a reasonable range [ $13.05 < \log(M_{\text{halo}}) < 14.58$ ] of parameter solutions from Table 4 in Yang et al. (2009). To quantify the systematic errors associated with the individual galaxy stellar mass measurements, we calculate the group stellar masses using the 2.5 and 97.5 percentile masses from the probability distribution of SED fits to our galaxies and find total group stellar masses an average of 0.5 and 2.0 times those found using the median galaxy masses, respectively, regardless of the total group stellar mass.

## 8. DYNAMICAL COMPLEXITY

### 8.1. Descriptions of Tests

We search for dynamical complexity/substructure in our groups by applying the DS (Dressler & Shectman 1988) test as in Hou et al. (2012). The DS test uses both spatial and velocity information in order to identify substructure. A thorough discussion of this test and its application can be found in Hou et al. but a brief discussion of our methodology follows. We begin with the mean velocity and velocity dispersion ( $\bar{v}$ ,  $\sigma$ ) for each group having  $n$  member galaxies. Then for each galaxy  $i$  in the group, we select it and a number of its nearest neighbors,  $N_{\text{nn}}$ , and compute their mean velocity  $v_{\text{local}}^i$  and velocity dispersion  $\sigma_{\text{local}}^i$ . From these we compute

$$\delta_i^2 = \left( \frac{N_{\text{nn}} + 1}{\sigma^2} \right) [(\bar{v}_{\text{local}}^i - \bar{v})^2 + (\sigma_{\text{local}}^i - \sigma)^2], \quad (6)$$

where  $1 \leq i \leq n_{\text{members}}$  and  $N_{\text{nn}} = \sqrt{n_{\text{members}}}$ . The DS  $\Delta$  statistic is then calculated as follows:

$$\Delta = \sum_{i=1}^N \delta_i, \quad (7)$$

where  $N$  is the total number of galaxies in the group.

100,000 Monte Carlo models are then run to calibrate the  $\Delta$  statistic for each group. Each Monte Carlo model is made by randomly shuffling the velocities among the group galaxies. Then a probability  $P$  is defined as the fraction of the total number of Monte Carlo models of the group that have  $\Delta$ 's larger than the true value of the group.  $P \approx 1.0$  means that the group contains no substructure, while  $P \approx 0.0$  indicates that the group contains statistically significant substructure. For a group to be defined as having substructure, we require  $P < 0.01$ .

**Table 9**  
Summary of Dynamical Complexity Test Results

	AD 1 Mpc	DS 1 Mpc	AD $r_{200,\sigma}$	DS $r_{200,\sigma}$	AD $r_{200,X}$	DS $r_{200,X}$
X-ray <sup>a</sup>	7 of 19	4 of 19	6 of 14	4 of 14	1 of 11	0 of 11
Optical	5 of 19	3 of 19	4 of 12	1 of 12	3 of 10	0 of 10

**Notes.** Column description: number of systems meeting dynamical complexity criterion per total number tested for X-ray and optical systems in each radial cut.

<sup>a</sup> Quality 1 & 2 systems only.

Another method of identifying dynamical complexity within groups is to search for deviations from a Gaussian velocity distribution. We use the AD test to classify velocity distributions as non-Gaussian as in Hou et al. (2009), and show that the test is reliable and robust for group-sized systems. A detailed analysis of the AD test is given in Hou et al. (2009), but we give a brief description of the statistic here. The AD statistic is a goodness-of-fit test that compares the cumulative distribution function (CDF) of ordered data to a model empirical distribution function (EDF), which in our case is a Gaussian EDF. This comparison is done using the following computing formulae (D'Agostino & Stephens 1986)

$$A^2 = -n - \frac{1}{n} \sum_{i=1}^n (2i-1)(\ln \Phi(x_i) + \ln(1 - \Phi(x_{n+1-i}))), \quad (8)$$

$$A^{2*} = A^2 \left( 1 + \frac{0.75}{n} + \frac{2.25}{n^2} \right), \quad (9)$$

where  $x_i \leq x < x_{i+1}$ ,  $\Phi(x_i)$  is the CDF of the hypothetical underlying distribution. Probabilities for the AD test are then computed using

$$\alpha = a \exp(-A^{2*}/b), \quad (10)$$

where  $a = 3.6789468$  and  $b = 0.1749916$ , and both factors are determined via Monte Carlo methods (Nelson 1998). A system is then considered to have a non-Gaussian velocity distribution, and therefore dynamical complexity, if its computed  $\alpha$  value is less than 0.01, corresponding to a 99% confidence level.

Hou et al. find both tests to be reliable for groups with 10 or more members, thus we apply them only to those groups in our samples which meet this criterion. Tests using mock catalogs indicate that this criterion, combined with the requirement of a probability less than 0.01, results in a false positive rate of 1% and 5% for the AD and DS tests, respectively.

### 8.2. Effect of Dynamical Complexity

Table 9 summarizes our results for both X-ray and optical groups, giving the number of systems where dynamical complexity was identified per the systems tested for each test and radial cut. In general, we find the least amount of dynamical complexity when we employ an X-ray-based  $r_{200}$  cut to our systems. In fact the DS test fails to find significant substructure for any group with this radial cut applied. When we use the, normally larger, 1 Mpc and velocity dispersion based radial cuts we find significantly more dynamical complexity. The latter cut yields the highest fraction of both non-Gaussian (AD) and substructure (DS) groups.

Figure 6 shows the results for both substructure tests for X-ray-selected system XR14h09. Substructure is detected in

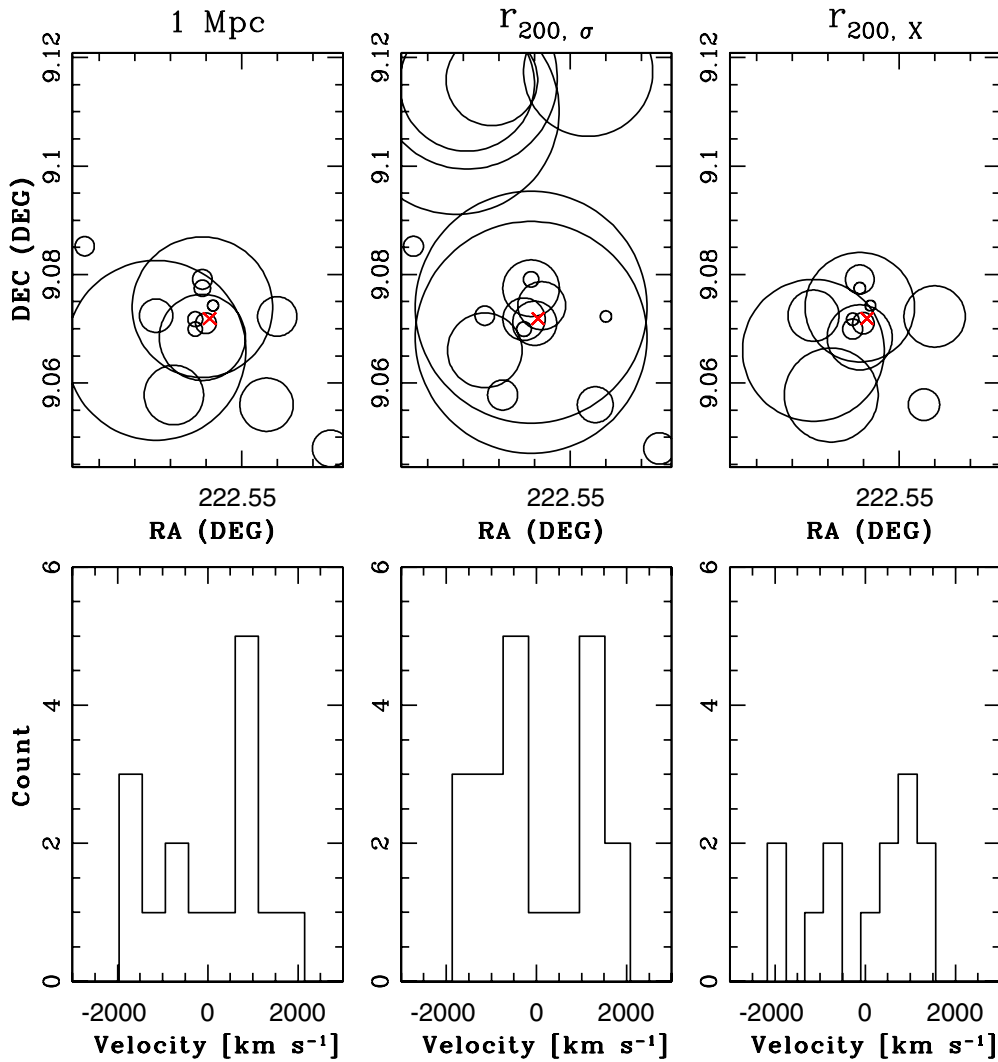


**Figure 6.** Results of substructure tests for group XR14h09. Top panel: Dressler & Shectman (1988) “bubble plots” where the galaxy symbols scale with  $\exp(\delta_i)$  for 1 Mpc,  $r_{200, \sigma}$ , and  $r_{200, X}$  radial cuts. The DS test finds substructure only in the case of an  $r_{200, \sigma}$  radial cut. Bottom panel: histogram of the velocity distribution for the same radial cuts as above. Non-Gaussianity (dynamical complexity) is detected using the AD test at all radial cuts.

(A color version of this figure is available in the online journal.)

this group at all radial cuts by the AD test and for the  $r_{200, \sigma}$  cut case according to the DS test. The top panel of Figure 6 shows DS “bubble plots” for this group for each of the three radial cuts. In a “bubble plot,” each galaxy in the group is plotted at its spatial position and is represented by a symbol whose size scales with its  $\delta_i$  value. Larger symbols indicate larger deviations in the local kinematics compared to the global values, and a “local grouping” of galaxies with similarly large symbols may indicate a kinematically distinct system. The  $r_{200, \sigma}$  cut plot shows such a congregation at a declination of  $\sim 9^{\circ}115$ .

The DS test fails to detect substructure for all groups when an X-ray-based  $r_{200}$  radial cut is applied. Assuming substructure is preferentially located at the outskirts of groups, this supports the hypothesis that an X-ray-based  $r_{200}$  cut is the one most likely to be tracing the virialized core of the system. Figure 7 looks more closely at this  $r_{200, X}$  cut, comparing the “real” velocity dispersions *measured* for quality 1 & 2 X-ray systems within the X-ray defined  $r_{200}$  to the velocity dispersion for the same systems if  $\sigma$  were instead *computed* by substituting  $r_{200, X}$  into Equation (4) and rearranging to get  $\sigma$ . The latter results in a much tighter range in velocity dispersions. Very low velocity dispersions are not possible when inferred from  $L_X$  due to

the X-ray detection limit but measured  $\sigma$  can be much larger than that inferred from the X-ray measurements. This implies that dynamical complexity may inflate velocity dispersion even within an X-ray-derived  $r_{200}$  but this is confirmed by the AD test in only a single case.

The differences in  $\sigma$ —and thus dynamical mass—*measurements* within the different radial cuts are, however, small. Stellar mass measurements though may be biased since larger radial cuts will always result in larger or equivalent stellar masses.

Although our X-ray imaging may not be deep enough to detect X-ray “substructure” in the majority of our systems, a pair of X-ray detected systems, XR21h06 and XR21h07, does appear to be one clear case of this in our sample. These groups lie at essentially the same redshift of 0.145 and appear as two separate peaks within an area of overlapping X-ray emission. The group XR21h07 corresponds to the center of optical group OP21h104. None of these groups have substructure detected using the AD or DS tests. This is especially surprising given a 1 Mpc radial cut as the membership overlaps so thoroughly in this case. If we relax our criterion to  $P \approx 0.06$ , XR21h06 would have substructure detected by the DS test in the case of all radial cuts and XR21h07

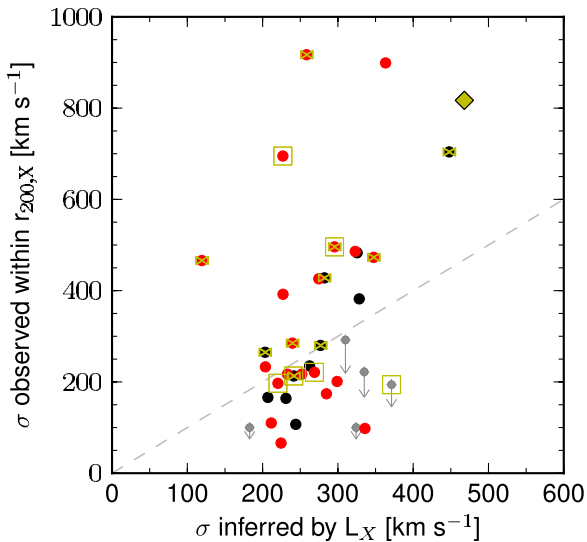


**Figure 7.** Velocity dispersions for quality 1 & 2 X-ray-selected systems (black and red filled circles, respectively) measured within  $r_{200,X}$  and calculated as in Equation (4) using  $r_{200,X}$ . Upper limits are shown in gray. Yellow bow-ties indicate systems tested for substructure. Filled yellow diamonds and squares indicate systems with substructure according to AD and DS tests, respectively. All substructure results shown here are for the  $r_{200,X}$  radial cut case. Open yellow squares show groups in X-ray confused regions. A 1:1 line is shown in dashed gray.

(A color version of this figure is available in the online journal.)

in the case of an X-ray-based  $r_{200}$  cut. OP21h104 would also have substructure detected via the DS test if the criterion was relaxed and an X-ray-based  $r_{200}$  cut employed. If these groups are merging in the plane of the sky, it is doubtful substructure would be detected by the DS test. Although the AD and DS tests have been shown to be reliable in most cases, there are certain scenarios in which either/both could fail and one such example is a merger in the plane of the sky. Since the aforementioned tests essentially look for deviations in the velocity distribution, these types of mergers may not have substructure with significant (or detectable) differences in velocity (e.g., Pinkney et al. 1996). Further discussion of false negatives for the DS test and the effect of superposition for massive GECC groups can be found in Hou et al. (2012).

### 9. $L_X$ - $\sigma$ RELATION

The X-ray-luminosity-velocity-dispersion ( $L_X$ - $\sigma$ ) relation is shown in Figure 8 for X-ray and optically selected groups with all radial cuts. In order to define the linear best fit for these relations while accounting for the errors in both  $L_X$  and  $\sigma$ , we choose a Bayesian approach as in Kelly (2007). Specifically, we use the LINMIX\_ERR IDL code of Kelly (2007) to determine the slope  $m$ , intercept  $c$ , and intrinsic scatter  $s$  of the relation  $\log(L_X) = m \times \log(\sigma) + c + \epsilon$ , where  $\epsilon$  is a random variable with variance equal to the square of the intrinsic scatter ( $s^2$ ). The Kelly method allows measurement errors to be treated as independent and log-normal and assumes that the intrinsic scatter in the dependent variable is Gaussian and the intrinsic distribution of the independent variables can be well approximated by a combination of Gaussians. The publicly available LINMIX\_ERR code constructs Monte Carlo Markov Chains (Gilks et al. 1996; Christensen & Meyer 2000) to draw random parameter sets from the probability distributions, the maxima of the distributions of these draws representing the best-fit values. Note the probability distribution can be asymmetric.

We compute  $1\sigma$  uncertainties using 15.9 and 85.1 percentile values of all fit quantities. Using the resultant slope, intercept, and intrinsic scatter, and their uncertainties, we shall search for increased scatter/outliers from the relation, attempting to tie this to an observable property of the outlying groups.

For the X-ray groups, we perform this best-fit analysis for quality 1, 1 & 2, and 1, 2, & 3 groups, respectively, and for each radial cut excluding those with upper limits on  $L_X$  and/or  $\sigma$ . As expected, the intrinsic scatter in the relation tends to increase with the addition of the poorer quality groups. Additionally, we examine the effect of luminosity-weighted recentering for X-ray systems by recomputing the membership and velocity dispersion and find little change in  $\sigma$  and thus little difference in the  $L_X$ - $\sigma$  relation. The best-fit analysis is also performed for the optical systems for all radial cuts. For a given radial cut, the  $L_X$ - $\sigma$  best fits for  $Q = 1$  & 2 X-ray and optically selected systems are relatively similar but the relation found for  $Q = 1$  X-ray systems significantly steeper. For a fixed  $L_X$ , the range in  $\sigma$  is much larger for  $Q = 2$  than for  $Q = 1$  X-ray systems. Additionally, the higher  $\sigma$   $Q = 2$  groups tend to lie well off the relation and exhibit dynamical complexity. The intrinsic scatter for the optical groups is larger than that found for the quality 1 X-ray groups, regardless of the quality cut applied, but generally comparable or less than that for the quality 1 & 2 X-ray systems. Note that most optical systems are excluded from the fitting due to their  $L_X$  measurement limits. We provide the  $L_X$ - $\sigma$  slope, intercept, and intrinsic scatter, and their uncertainties, for the optical and high-quality X-ray systems for each of the different radial cuts in Table 10.

We plot for comparison the  $L_X$ - $\sigma$  relation derived from two different samples: the Mulchaey et al. (2003) sample of groups at  $z \approx 0$  and the Rykoff et al. (2008) maxBCG sample of clusters at  $0.1 \leq z \leq 0.3$ . We show these comparisons as dashed and dotted lines in Figure 8 and find no evidence for deviation from the assumed evolution of this relation with redshift. The slope in our relation however clearly depends on the groups selected (i.e., optical, X-ray  $Q = 1$ , or X-ray systems). For example, our slope for the highest quality X-ray-selected systems is very similar to the  $2.56 \pm 0.56$  found by Osmond & Ponman for the GEMS group sample (Osmond & Ponman 2004), while the slopes for our  $Q = 1$  & 2 X-ray systems and optical systems with an X-ray-derived  $r_{200}$  are in relatively good agreement with that of Jeltema et al. (2008,  $m = 1.7 \pm 0.4$ ) though their relation is calculated within  $r_{500,X}$  and the groups used are on average more massive than ours. The group selection then drives a range of slopes which are consistent with both of these results. In general, our work supports the findings that the  $L_X$ - $\sigma$  relation for groups is shallower than that for clusters (Mahdavi & Geller 2001; Xue & Wu 2000) where the relation has been found to agree well with the bolometric X-ray luminosity  $\propto \sigma^4$  predicted by self-similar evolution (e.g., Horner 2001; Zhang et al. 2011).

Note that several of the most significant outliers at high mass in these relations show substructure (marked as filled yellow diamonds and squares). Given a  $\sigma$ -based  $r_{200}$  radial cut, all systems with a velocity dispersion greater than  $500 \text{ km s}^{-1}$  show dynamical complexity implying that these high values may be overestimated. This translates to a dynamical mass of  $\sim 10^{14.1} M_\odot$ .

High-quality X-ray groups in X-ray confused regions (quality 1.5 or 2.5, shown as open yellow squares in Figure 8) do not seem to be preferentially high in X-ray luminosity. For both X-ray (quality 1 & 2) and optical systems, the use of a  $\sigma$ -derived  $r_{200}$  cut results in the largest scatter in the  $L_X$ - $\sigma$

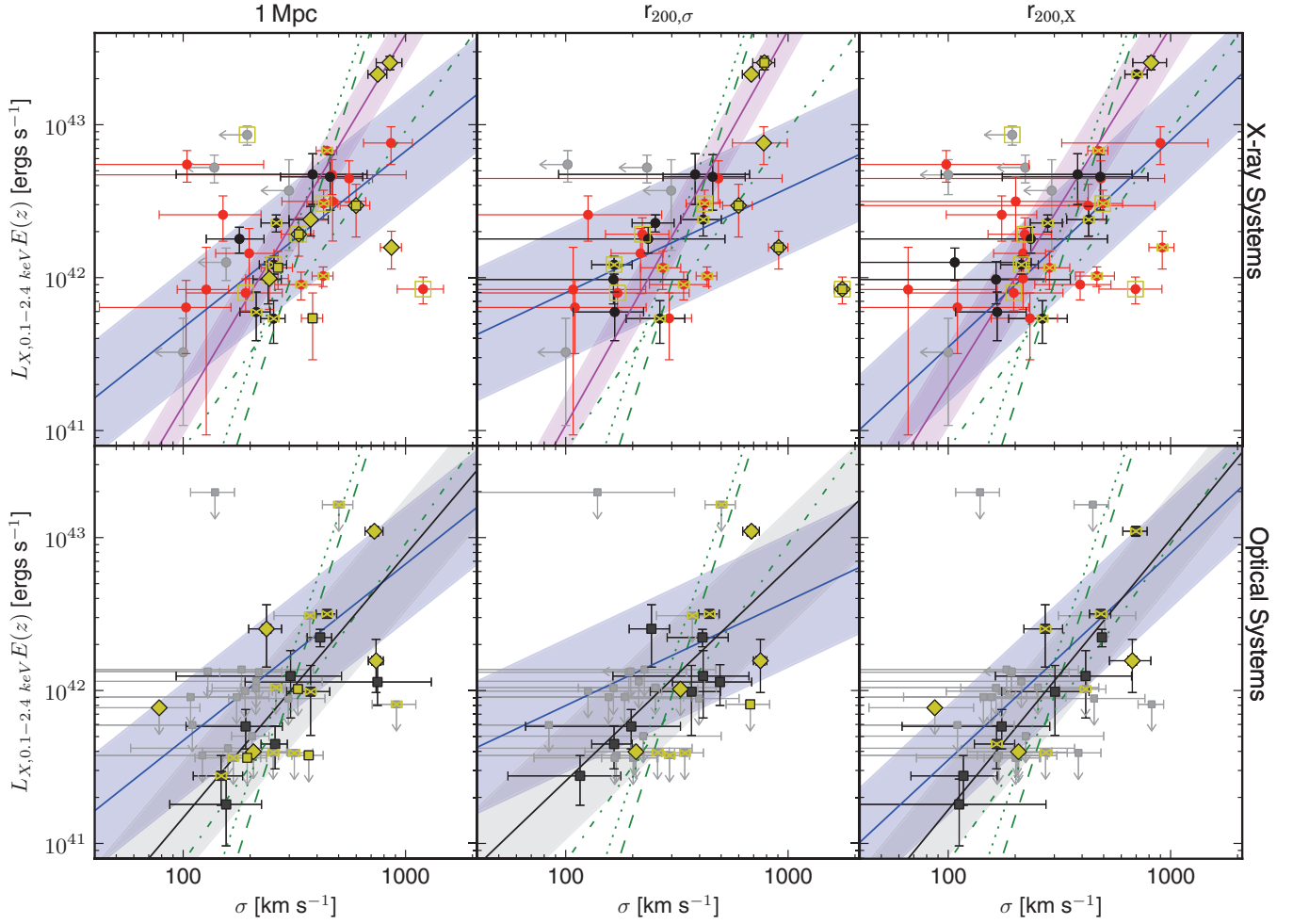


**Figure 8.**  $L_X$ - $\sigma$  relation for quality 1 & 2 (black and red circles, respectively) X-ray-selected systems (top) and optical systems (bottom) for all radial cuts. Gray arrows indicate limits. Dashed and dot-dashed green lines show  $z \sim 0$  sample fits (Mulchaey et al. 2003) while the dotted line is a  $z \sim 0.25$  sample (Rykoff et al. 2008). Bayesian best fits for quality 1 (magenta) and quality 1 & 2 (blue) X-ray and optical systems (black) are shown with filled region representing the scatter. Yellow bow-ties show systems tested for substructure. Filled yellow diamonds and squares indicate systems with substructure according to AD and DS tests, respectively. Open yellow squares show groups in X-ray confused regions.

**Table 10**  
 $L_X$ - $\sigma$  Relation Bayesian Best Fits

		$m$	$c$	$s$
X-ray $Q = 1$	1 Mpc	$2.5816 \pm_{-0.4435}^{+0.4600}$	$35.872 \pm_{-1.1891}^{+1.1489}$	$0.1884 \pm_{-0.0916}^{+0.1286}$
	$r_{200,\sigma}$	$2.3432 \pm_{-0.6154}^{+0.5045}$	$36.608 \pm_{-1.3824}^{+1.4957}$	$0.2592 \pm_{-0.1286}^{+0.1781}$
	$r_{200,X}$	$2.4044 \pm_{-0.6071}^{+0.5879}$	$36.341 \pm_{-1.5406}^{+1.5298}$	$0.2266 \pm_{-0.1126}^{+0.1639}$
X-ray $Q = 1 \& 2$	1 Mpc	$1.1539 \pm_{-0.3793}^{+0.3806}$	$39.364 \pm_{-0.9635}^{+0.9873}$	$0.3703 \pm_{-0.0533}^{+0.0654}$
	$r_{200,\sigma}$	$0.6844 \pm_{-0.3491}^{+0.3535}$	$40.532 \pm_{-0.9149}^{+0.9050}$	$0.4303 \pm_{-0.0613}^{+0.0821}$
	$r_{200,X}$	$1.3529 \pm_{-0.4650}^{+0.4249}$	$38.839 \pm_{-1.0722}^{+1.2093}$	$0.3533 \pm_{-0.0548}^{+0.0664}$
Optical	1 Mpc	$1.7125 \pm_{-0.5902}^{+0.5883}$	$37.769 \pm_{-1.5344}^{+1.4878}$	$0.3577 \pm_{-0.1034}^{+0.1554}$
	$r_{200,\sigma}$	$1.3628 \pm_{-0.6117}^{+0.6351}$	$38.691 \pm_{-1.6341}^{+1.5328}$	$0.3779 \pm_{-0.1081}^{+0.1568}$
	$r_{200,X}$	$1.7822 \pm_{-0.5350}^{+0.6019}$	$37.665 \pm_{-1.5601}^{+1.3516}$	$0.2994 \pm_{-0.1119}^{+0.1614}$

**Notes.** Column description: Bayesian best-fit slope ( $m$ ) and uncertainties (Column 1); intercept ( $c$ ) and uncertainties (Column 2); and intrinsic scatter ( $s$ ) and uncertainties (Column 3) of the relation  $\log(L_X) = m \times \log(\sigma) + c + \epsilon$ , where  $\epsilon$  is a random variable with variance equal to  $s^2$ .

**Table 11**  
 $L_X$ - $\sigma$  Relation Bayesian Best Fits with Groups Subdivided at  $N_{\text{mem}} = 10$

		$m$		$c$		$s$	
		$N_{\text{mem}} \geq 10$	$N_{\text{mem}} < 10$	$N_{\text{mem}} \geq 10$	$N_{\text{mem}} < 10$	$N_{\text{mem}} \geq 10$	$N_{\text{mem}} < 10$
X-ray $Q = 1$	1 Mpc	$2.7432 \pm_{-0.4385}^{+0.4646}$	...	$35.410 \pm_{-1.1809}^{+1.1414}$	...	$0.1970 \pm_{-0.0971}^{+0.1726}$	...
	$r_{200,\sigma}$	$2.6415 \pm_{-1.9239}^{+3.1382}$	$1.3271 \pm_{-1.6924}^{+2.6441}$	$35.715 \pm_{-8.6822}^{+5.0870}$	$39.005 \pm_{-6.3108}^{+4.1871}$	$0.9425 \pm_{-0.5930}^{+3.2969}$	$0.4254 \pm_{-0.2154}^{+0.4463}$
	$r_{200,X}$	$2.7481 \pm_{-0.9573}^{+1.2929}$	$1.0101 \pm_{-1.6856}^{+2.3692}$	$35.446 \pm_{-3.4051}^{+2.5106}$	$39.823 \pm_{-5.5660}^{+4.0695}$	$0.4255 \pm_{-0.2428}^{+0.6163}$	$0.4703 \pm_{-0.2401}^{+0.5544}$
X-ray $Q = 1 \& 2$	1 Mpc	$1.8992 \pm_{-0.5434}^{+0.5452}$	$0.4102 \pm_{-0.4068}^{+0.4228}$	$37.382 \pm_{-1.4129}^{+1.4192}$	$41.365 \pm_{-1.0802}^{+1.0160}$	$0.3753 \pm_{-0.0763}^{+0.0981}$	$0.3720 \pm_{-0.0828}^{+0.1108}$
	$r_{200,\sigma}$	$0.6790 \pm_{-0.6583}^{+0.6856}$	$1.3627 \pm_{-5.1712}^{+2.8705}$	$40.551 \pm_{-1.8619}^{+1.7749}$	$38.960 \pm_{-6.8315}^{+12.436}$	$0.5935 \pm_{-0.1215}^{+0.1781}$	$0.2772 \pm_{-0.1225}^{+0.1314}$
	$r_{200,X}$	$1.6872 \pm_{-0.8285}^{+0.9013}$	$0.7869 \pm_{-1.0626}^{+1.0804}$	$37.982 \pm_{-2.3799}^{+2.2048}$	$40.305 \pm_{-2.6528}^{+2.5923}$	$0.5120 \pm_{-0.1263}^{+0.1885}$	$0.3212 \pm_{-0.0772}^{+0.0921}$
Optical	1 Mpc	$1.3423 \pm_{-1.7528}^{+1.6965}$	$1.6129 \pm_{-1.2340}^{+1.5271}$	$38.801 \pm_{-4.4914}^{+4.6197}$	$37.955 \pm_{-3.8198}^{+2.9675}$	$0.7150 \pm_{-0.2929}^{+0.7264}$	$0.4429 \pm_{-0.2305}^{+0.5366}$
	$r_{200,\sigma}$	$1.1933 \pm_{-1.4801}^{+1.4007}$	$1.1905 \pm_{-2.8864}^{+3.6719}$	$39.256 \pm_{-3.6676}^{+3.8189}$	$38.973 \pm_{-9.4757}^{+7.0081}$	$0.6992 \pm_{-0.2927}^{+0.7714}$	$0.6732 \pm_{-0.4107}^{+1.8007}$
	$r_{200,X}$	$1.6430 \pm_{-1.1730}^{+1.1719}$	$1.2470 \pm_{-1.8734}^{+1.7510}$	$38.067 \pm_{-3.0917}^{+3.0628}$	$38.922 \pm_{-4.4495}^{+4.3277}$	$0.5334 \pm_{-0.2385}^{+0.5298}$	$0.7305 \pm_{-0.4627}^{+1.5954}$

**Notes.** Column description: Bayesian best-fit slope ( $m$ ) and uncertainties (Columns 1 and 2); intercept ( $c$ ) and uncertainties (Columns 3 and 4); and intrinsic scatter ( $s$ ) and uncertainties (Columns 5 and 6) of the relation  $\log(L_X) = m \times \log(\sigma) + c + \epsilon$ , where  $\epsilon$  is a random variable with variance equal to  $s^2$ . The first column of each quantity is for groups with at least 10 members while the second only includes those with less than this amount. Note that in the case of the quality 1 X-ray groups with a 1 Mpc radial cut, there is an insufficient number of groups with less than 10 members to perform robust fitting.

relation and looks to be biased toward giving higher dispersions for dynamically complex systems. The X-ray-derived  $r_{200}$  cut provides a relatively tight correlation even for optically selected systems. A 1 Mpc cut produces similarly tight fits for the good quality X-ray systems but is less well constrained than the X-ray radial cut for optical systems. This constant cut can extend beyond a physical  $r_{200}$  or lie within it and is biased large (small) for low (high) halo masses.

As velocity dispersions for systems having few members are less reliable (e.g., Zabludoff & Mulchaey 1998; Girardi & Mezzetti 2001), we performed additional Bayesian fitting to the  $L_X$ - $\sigma$  relation further dividing our subsamples into those with  $N_{\text{mem}} < 10$  and those with  $N_{\text{mem}} \geq 10$  and present the results in Table 11. Note that the latter subsample is comprised of all groups where dynamical complexity could be evaluated which are thus marked by yellow bow-ties or filled squares or diamonds in Figures 7 and 8. It is clear from Figure 8 that, for X-ray-selected groups, the low  $N_{\text{mem}}$  systems tend to have lower dispersion than the high  $N_{\text{mem}}$  groups at fixed  $L_X$  regardless of the radial cut applied. This indicates either that the dispersion and number of members correlates better with the group mass than  $L_X$  or that the dispersion is typically estimated lower with fewer members. Nonetheless, the overall fits are within the range of those found for the total population. As systems with few members also have large measurement errors in their velocity dispersions, they are consistent with a wide range of relations, while the high  $N_{\text{mem}}$  groups have smaller errors and thus import more stringent constraints on the best-fit relation. In this light, it is not surprising that similar results are produced.

## 10. TOTAL MASS MEASUREMENTS

Figure 9 presents the two “total” mass measures for our samples: the X-ray and dynamical mass measures. In this figure we show an X-ray-based  $r_{200}$  radial cut but, regardless of the radial cut applied, the disagreement between these measures increases for the average group, and the scatter decreases, with increasing dynamical mass. This is not unexpected, since the range in dynamical mass is much larger than in X-ray mass

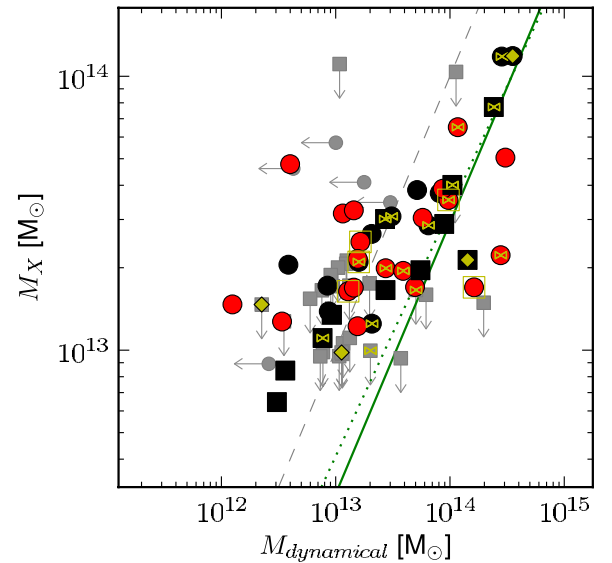


**Figure 9.**  $M_X$ - $M_{\text{dyn}}$  relation for quality 1 & 2 X-ray (black and red circles, respectively) and optical systems (black squares) within  $r_{200,X}$ . Gray arrows indicate limits. Yellow bow-ties show systems tested for substructure. Filled yellow diamonds and squares indicate systems with substructure according to AD and DS tests, respectively. Open yellow squares show groups in X-ray confused regions. A 1:1 line is shown in dashed gray. Girardi et al. (1998) weighted and bisecting regression lines are shown for comparison as green solid and dotted lines, respectively.

(A color version of this figure is available in the online journal.)

(recall Figure 7). For  $\sigma$  and 1 Mpc radial cuts, the dynamical mass may be inflated by overestimates of velocity dispersion in systems with dynamical complexity. In general, X-ray masses are preferable, better discerning the virialized core of the system, but, for systems undetected in X-rays, this tracer of halo mass is unavailable. Girardi et al. (1998) find, for an inhomogeneous sample of clusters, good agreement between virial and X-ray masses. We show in Figure 9 their weighted regression lines for comparison. We find our masses are less and less in agreement with increasing total mass. Dynamical masses for massive

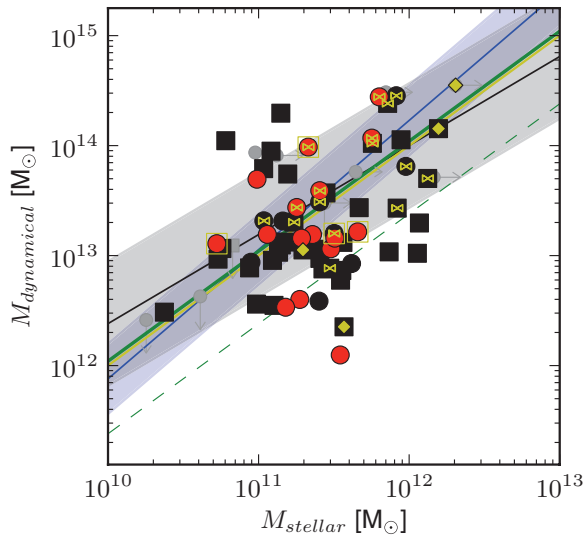


**Figure 10.**  $M_{\text{dyn}}-M_{\text{stellar}}$  relation for quality 1 & 2 X-ray (black and red circles, respectively) and optical systems (black squares) within  $r_{200,X}$ . Gray arrows indicate limits. Yellow bow-ties show systems tested for substructure. Filled yellow diamonds and squares indicate systems with substructure according to AD and DS tests, respectively. Open yellow squares show groups in X-ray confused regions. Bayesian best fits for the X-ray systems (blue) and optical systems (black) are shown with filled region representing the scatter. Constant stellar mass fractions of 0.009 and 0.042 are shown in green solid and dashed lines, respectively, and correspond to the fractions found for  $M_{200}$  halo masses of  $14.9$  and  $13.7 M_{\odot}$  by Andreon (2010). The average 1% fraction found by Balogh et al. (2011a) within  $r_{500}$  for nearby low-mass clusters is shown in yellow.

(A color version of this figure is available in the online journal.)

systems might be improved with better dynamical modeling (e.g., “caustic masses,” e.g., Andreon 2010, Serra et al. 2011, etc.), but such estimates are only possible when the number of spectroscopic galaxies in and around the group (cluster) is high.

## 11. MASS IN STARS

### 11.1. Stellar versus “Total” Group Mass

The dynamical and group stellar masses are compared in Figure 10. Stellar mass fractions for two different group halo masses from Andreon (2010) are overplotted for comparison. Our best fits are similar to the stellar mass fraction of 0.009 found by Andreon for a  $10^{14.9} M_{\odot}$  halo. To derive total stellar masses, Andreon integrates the total luminosity function for all red galaxies in a cluster, assuming that, in the cluster regime, blue galaxies contribute little to the overall luminosity, and assumes a dynamical  $M/L$  from Cappellari et al. (2006). Our results are in good agreement average 1% stellar to dynamical mass fraction within  $r_{500}$  found by Balogh et al. (2011a) for a sample of low-mass nearby clusters.

Figure 11 shows the stellar and X-ray masses of all of our systems. We compare relations found by Yang et al. (2009) for a low-redshift sample of groups selected from SDSS, by Giodini et al. (2009) for  $0.1 \leq z \leq 1$  COSMOS X-ray detected groups, and by Balogh et al. (2011a) for nearby clusters and find relatively good agreement. For the latter comparison, we shift the Giodini relation, which was computed for an  $r_{500}$  radial cut assuming a simple conversion of  $M_{200} \sim M_{500}/0.7$  and shifted by 0.25 dex to account for the difference in assumed IMFs (see Leauthaud et al. 2012). Note that Giodini et al. integrate down to a stellar mass limit of  $10^8 M_{\odot}$  which, when compared to our limit of  $10^{10} M_{\odot}$ , means their total group stellar masses

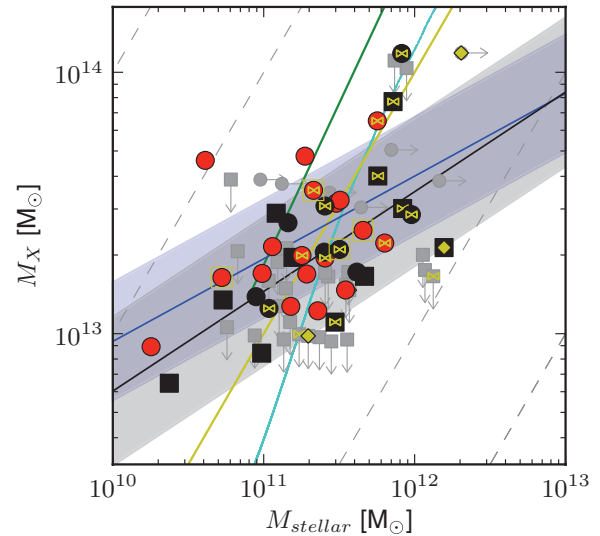


**Figure 11.**  $M_X-M_{\text{stellar}}$  relation for quality 1 & 2 X-ray (black and red circles, respectively) systems within  $r_{200,X}$ . Gray arrows indicate limits. Yellow bow-ties show systems tested for substructure. Filled yellow diamonds and squares indicate systems with substructure according to AD and DS tests, respectively. Open yellow squares show groups in X-ray confused regions. Bayesian best fits for the X-ray systems (blue) and optical systems (black) are shown with filled region representing the scatter. Yang et al. (2009) data are overplotted in cyan, Giodini et al. (2009) relation is shown in green, and the average 1% fraction found within  $r_{500}$  for nearby low-mass clusters by Balogh et al. (2011a) shown in yellow. Lines of constant mass are shown as gray dashed lines.

(A color version of this figure is available in the online journal.)

should be slightly higher. At lower X-ray mass, our derived best linear fit indicates significantly lower stellar masses than Yang or Giodini. However, the latter notes that, in this low X-ray mass region, their stellar masses can range by a factor of 10 at a fixed total mass and that the logarithmic intrinsic scatter of their relation is of order 35%. Our results well match the average 1% stellar to X-ray mass fraction found by Balogh et al. (2011a) for a sample of low-mass nearby clusters within  $r_{500}$ .

Both the  $M_{\text{dyn}}-M_{\text{stellar}}$  and  $M_X-M_{\text{stellar}}$  relations show a wide range in stellar mass for a given “total” mass especially considering the limits. With a  $\sigma$ -derived  $r_{200}$ , the  $M_{\text{dyn}}-M_{\text{stellar}}$  relation *appears* to improve. However, this is merely due to the increased range in velocity dispersion and thus  $M_{\text{dyn}}$  with most high- $\sigma$  groups exhibiting dynamical complexity (recall Figure 8). This drives up  $M_{\text{dyn}}$  but can also increase  $M_{\text{stellar}}$  due to the increased membership resulting from larger  $r_{200}$ . Therefore, we choose not to show the  $\sigma$ -derived  $r_{200}$  cut version of this relation as its relative tightness is misleading. The  $M_X-M_{\text{stellar}}$  relations behave similarly when comparing the differently defined radial cuts.

To determine if the scatter in  $M_{\text{stellar}}$  given fixed total mass may be related to the dominance of the most massive galaxy (MMG), we first identify the MMG in each group and examine the offset of this galaxy from the group center. Figure 12 shows the histogram of offsets and the offset versus the total (X-ray) system mass. The MMG generally lies near the group center regardless of whether an X-ray or luminosity-weighted center is used. With the exception of a single system, groups with higher X-ray mass ( $M_X \gtrsim 3.5 \times 10^{13} M_{\odot}$ ) have the MMG within the inner third of the X-ray-derived  $r_{200}$ . This corresponds to a distance of less than 200 kpc from the group center (nearer allowing for centering accuracy, see Figure 4). For lower mass systems, there is a much greater scatter in the offset of the MMG. The group with its MMG at greatest offset from the center is

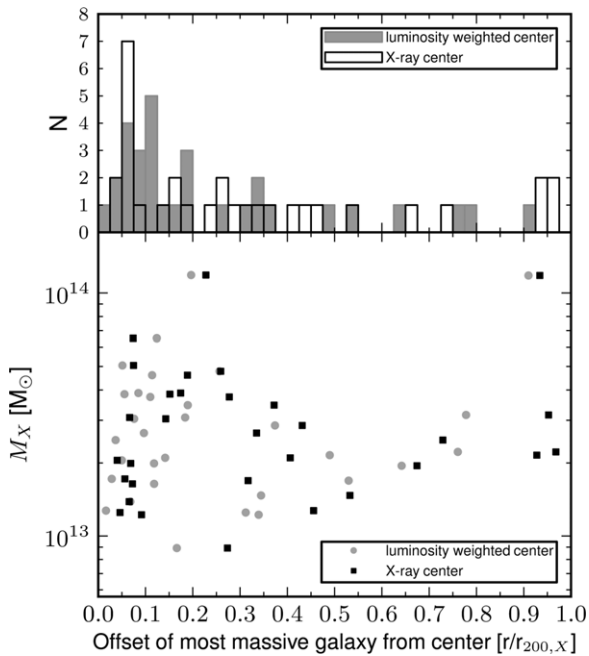


**Figure 12.** Histogram of the offset of the most massive galaxy from the group center (top) and vs. total (X-ray) group mass (bottom). Offsets from X-ray centers are shown as black hashed histogram and black squares, and luminosity-weighted centers are shown as gray histogram and circles.

XR21h14 (OP21h138), a massive group with two bright stars near the (projected) center. It is likely that the complication introduced to the photometry in this area due to the presence of these stars may be obscuring the actual MMG for this group. The stellar mass contributed by the MMGs does decrease with increasing total stellar mass, regardless of radial cut or choice of group center from an average fraction of  $\sim 0.5$  at  $3 \times 10^{10} M_{\odot}$  to  $\lesssim 0.2$  at  $2 \times 10^{12} M_{\odot}$ . In the cluster regime, Sanderson et al. (2009) found that the offset of the BCG relates both to activity in that galaxy and to the dynamical state of the cluster itself. A full study of our BGGs (or MMGs) which includes correlation of offsets with emission properties as in Sanderson and also exploration of issues such as multiple component BGGs (as in Jeltema et al. 2007) would be an interesting addition to future work on galaxy properties.

### 11.2. Stellar Mass Fractions

Using the X-ray mass to represent the total halo mass, our best fits for both the high-quality X-ray and optically selected systems indicate almost constant fractions ( $M_{\text{stellar}}/M_X$ ) of  $\sim 0.011$ , independent of halo mass ( $M_X$ ). This is different from the *mean* fraction  $M_{\text{stellar}}/M_X \sim 0.014$  with logarithmic standard deviation of 0.398. Recall that we integrate our stellar mass down to  $10^{10} M_{\odot}$ . Using dynamical mass instead as the total group mass results in a mean fraction of  $\sim 0.022$ . Examining the  $M_{\text{dyn}}-M_{\text{stellar}}$  best fits, the fraction is similar to the  $\sim 0.009$  found by Andreon for a  $10^{14.9} M_{\odot}$  halo. Giodini et al. find that the stellar mass fraction associated with galaxies within  $r_{500}$  decreases with increasing total mass as  $M_{500}^{-0.26 \pm 0.04}$ . We do not find a similar relation but note that the relation found by Giodini et al. breaks down when clusters are excluded.

Figure 13 shows the stellar mass fraction versus the total (X-ray) system mass given an X-ray-based  $r_{200}$  cut for the total stellar mass and mass of the MMG. The mean contribution of the MMG to the total system mass ( $M_{\text{stellar}}^{\text{MMG}}/M_X$ ) including both

quality 1 & 2 X-ray and optically selected systems is  $\sim 0.004$ . In addition to constant lines approximating our mean stellar mass fractions for an X-ray-based halo mass, we show the fractions found by Giodini et al. (2009) for their COSMOS sample of groups, Balogh et al. (2011a) within  $r_{500}$  for their nearby low-mass galaxy clusters, the Leauthaud et al. (2012)  $z \sim 0.37$  COSMOS-derived sample of groups and clusters, and the fraction including intracluster light (ICL) within  $r_{500}$  from the Gonzalez et al. (2007) cluster sample. We again shift the Giodini relation to account for a difference in IMF. Additionally, the fractions found by Leauthaud by dividing the group population into central and satellite galaxies are shown. In the cluster regime, stellar mass fractions are not universal, but generally decrease with increasing cluster mass (e.g., Ramella et al. 2004; Eke et al. 2005; Giodini et al. 2009). We find our fraction to be significantly lower than the fraction including ICL found by Gonzalez et al. (2007) with this divergence increasing with decreasing X-ray mass. We find many more systems at lower stellar mass fractions than do Giodini et al. Our spectroscopic selection results in a larger scatter in the stellar mass fraction.

## 12. UNDERLUMINOUS GROUPS

Figure 14 (top panel) shows the  $M_{\text{stellar}}-L_X$  relations for X-ray and optical groups, respectively, with an X-ray-based  $r_{200}$  cut applied. We provide the best-fit slope, intercept, and intrinsic scatter, and uncertainties, for the reciprocal relation ( $L_X-M_{\text{stellar}}$ ) for the optical and high-quality X-ray systems for each of the different radial cuts in Table 12. Note that errors in stellar mass are averaged in order to produce symmetric errors for input into the Kelly Bayesian best-fit procedure. The best-fit solutions for X-ray systems vary significantly between the quality 1 and quality 1 & 2 systems and between different radial cuts. Considering only the quality 1 X-ray systems, the 1 Mpc radial cut produces a relatively shallow relation, similar to that for optical and  $Q = 1$  & 2 X-ray system considering the very large intrinsic scatter, but both  $r_{200}$  based cuts for these highest quality systems are significantly steeper. Comparing the quality 1 & 2 X-ray systems only to that for the optical groups and taking the uncertainties into account, the best fit to the relations for both samples are similar. If the upper limits in X-ray luminosity were included, assuming the luminosity is the value of the limit (the maximum possible), the optical groups would be on average comparatively *underluminous* in X-rays.

Including these limits, we perform the best fit again for our systems, splitting the entire population, including all optical systems and  $Q = 1$  & 2 X-ray systems, into three types of groups: “underluminous,” “normal,” and “overluminous” *relative to their stellar mass*. We define X-ray under- and overluminous groups as those which have lower/higher  $L_X$  than the best-fit value (including upper limits), minus/plus half the scatter ( $0.5s$ ). Those groups that are underluminous, having higher stellar masses and lower luminosities than the fit even including half the scatter, are marked by open magenta squares while the overluminous systems are marked similarly in cyan. Note that while groups with upper limits in X-ray luminosity are included in the underluminous group population, we exclude these from the overluminous subset as they may in fact be consistent with the relation.

Note that to further ensure the robustness of these results, the under- and overluminous groups were also defined relative to the best fit based on the X-ray ( $Q = 1$  & 2) systems and, though specific numbers changed, all qualitative results

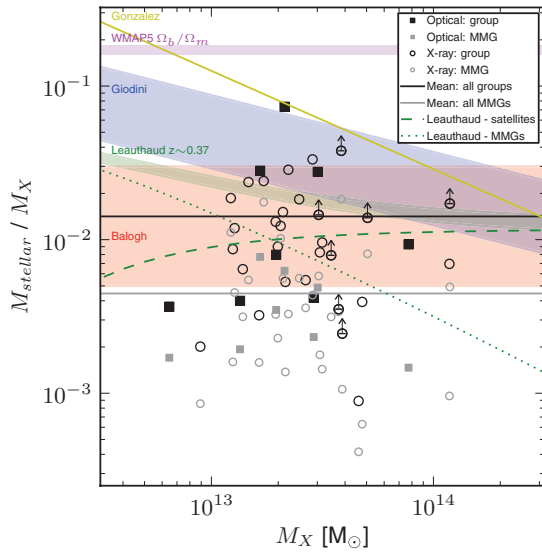


**Figure 13.** Stellar mass fraction vs. total mass. Black and gray circles indicate total and most massive galaxy fractions, respectively, for X-ray systems while squares indicate similar quantities for optical systems. The mean stellar mass fraction for our entire sample (high-quality X-ray and optical samples) is indicated by a black solid line and that of the MMG in gray. The Leauthaud et al. (2012)  $z \sim 0.37$  stellar mass fraction is shown in green with dotted green line indicating central and dashed green line indicating the contribution from satellite galaxies. The Giodini et al. (2009) COSMOS sample stellar mass fraction and its intrinsic scatter is shown in blue. The Balogh et al. (2011a) fraction measured within  $r_{500}$  is shown in red and the Gonzalez et al. (2007) in yellow. The baryon fraction from WMAP5 (Dunkley et al. 2009) is plotted in magenta.

remained consistent. However, using only the  $Q = 1$  groups for either of the  $r_{200}$  based cuts would result in a more cluster-like slope of the  $L_X - M_{\text{stellar}}$  relation (top left panel of Figure 14) and a significant difference in the population of groups defined as under- or overluminous.

Several of the outliers to the  $M_{\text{stellar}} - L_X$  relation, including an underluminous optical and the most overluminous X-ray group—which are also the systems with the highest stellar mass—show substructure. However, some of the groups with  $\geq 10$  members (marked as yellow bow-ties) do not show evidence of substructure from either the AD or DS test and are among the most significant outliers from this relation.

The bottom panel of Figure 14 shows the  $M_{\text{dyn}} - L_X$  relations for X-ray and optical groups, respectively, with an X-ray-based  $r_{200}$  cut applied. Examining the positions of the underluminous systems, indicated by open magenta squares, their dynamical masses are not unusually low, spanning a wide range in  $M_{\text{dyn}}$ , and many of these underluminous groups do not exhibit significant dynamical complexity. Recall that the latter may lead to elevated velocity dispersions and overestimation of dynamical and group stellar mass. Groups with low X-ray luminosity relative to their stellar mass then do not exhibit particularly unusual dynamical characteristics. This may suggest a population of dynamically young groups which are just in the process of collapse.

Next we examine the median contribution of the MMG to the total group stellar mass ( $M_{\text{stellar}}^{\text{MMG}} / M_{\text{stellar}}$ ). Recall that  $M_{\text{stellar}}$  for all groups has had substantial incompleteness corrections

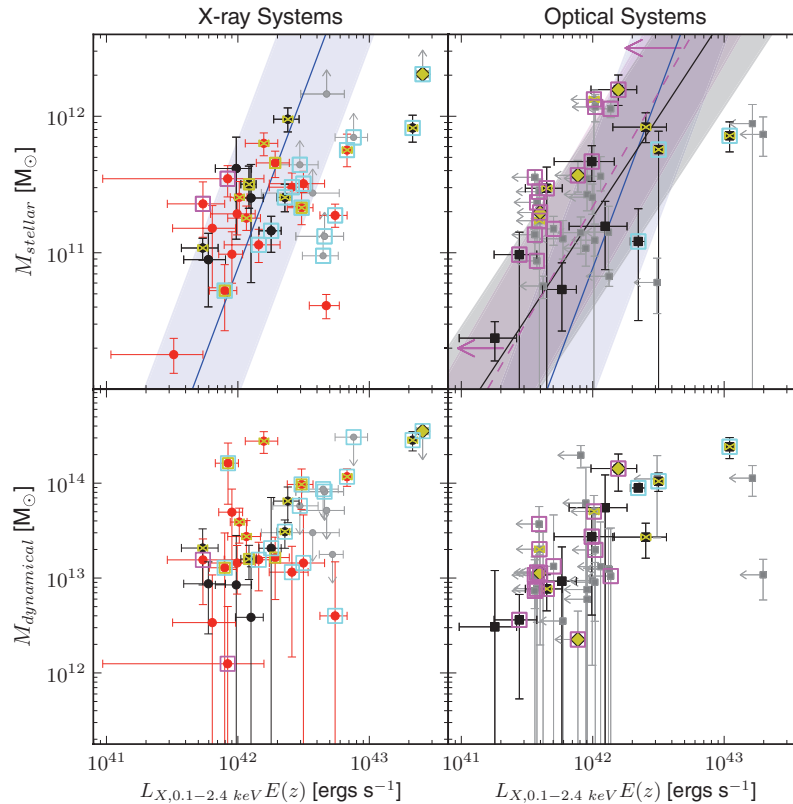


**Figure 14.** Top:  $M_{\text{stellar}} - L_X$  relation for X-ray-selected systems (left) and optical systems (right) with X-ray-based  $r_{200}$  cut applied. Bayesian best fits are shown in blue and black (X-ray and optical fits, respectively) with filled regions representing the scatter. Bayesian best fit for optical systems where upper limits on X-ray luminosity have been treated as detections is shown in magenta with filled region representing the scatter and magenta arrows reflecting that this relation is in reality likely shifted to lower X-ray luminosities. Bottom:  $M_{\text{dyn}} - L_X$  relation for X-ray (left) and optically (right) selected systems with X-ray-based  $r_{200}$  cut applied. Quality 1 & 2 X-ray-selected systems are shown as black and red circles, respectively, while optical systems are shown as black squares. Gray arrows indicate limits. Yellow bow-ties show systems tested for substructure. Filled yellow diamonds and squares indicate systems with substructure according to AD and DS tests, respectively. Open yellow squares show groups in X-ray confused regions. Open magenta and cyan squares indicate X-ray underluminous and overluminous systems, respectively.



**Table 12**  
 $L_X$ – $M_{\text{stellar}}$  Relation Bayesian Best Fits

		$m$	$c$	$s$
X-ray $Q = 1$	1 Mpc	$0.2506 \pm_{-0.8836}^{+0.9341}$	$39.184 \pm_{-11.047}^{+10.542}$	$0.6271 \pm_{-0.1676}^{+0.3061}$
	$r_{200,\sigma}$	$1.0128 \pm_{-0.3992}^{+0.4214}$	$30.463 \pm_{-4.9364}^{+4.6178}$	$0.3981 \pm_{-0.1378}^{+0.2403}$
	$r_{200,X}$	$1.0659 \pm_{-0.7725}^{+0.7493}$	$29.847 \pm_{-8.7808}^{+8.8896}$	$0.5017 \pm_{-0.1500}^{+0.2429}$
X-ray $Q = 1 \& 2$	1 Mpc	$0.1636 \pm_{-0.1759}^{+0.1822}$	$40.301 \pm_{-2.1560}^{+2.0875}$	$0.4057 \pm_{-0.0582}^{+0.0761}$
	$r_{200,\sigma}$	$0.4285 \pm_{-0.1564}^{+0.1563}$	$37.197 \pm_{-1.8303}^{+1.8092}$	$0.3228 \pm_{-0.0552}^{+0.0694}$
	$r_{200,X}$	$0.3903 \pm_{-0.1748}^{+0.1779}$	$37.749 \pm_{-2.0485}^{+1.9910}$	$0.3625 \pm_{-0.0544}^{+0.0647}$
Optical	1 Mpc	$0.5915 \pm_{-0.2970}^{+0.3093}$	$35.288 \pm_{-3.5627}^{+3.4474}$	$0.4661 \pm_{-0.1085}^{+0.1646}$
	$r_{200,\sigma}$	$0.5266 \pm_{-0.2653}^{+0.2603}$	$36.093 \pm_{-3.0718}^{+3.0918}$	$0.4010 \pm_{-0.1014}^{+0.1570}$
	$r_{200,X}$	$0.7034 \pm_{-0.3040}^{+0.2943}$	$34.042 \pm_{-3.3378}^{+3.4661}$	$0.4459 \pm_{-0.1188}^{+0.1849}$
Optical with upper limits	1 Mpc	$0.5161 \pm_{-0.1841}^{+0.1802}$	$36.081 \pm_{-2.0891}^{+2.1159}$	$0.3870 \pm_{-0.0521}^{+0.0648}$
	$r_{200,\sigma}$	$0.5198 \pm_{-0.1658}^{+0.1678}$	$36.089 \pm_{-1.9111}^{+1.9194}$	$0.3640 \pm_{-0.0566}^{+0.0679}$
	$r_{200,X}$	$0.5956 \pm_{-0.1789}^{+0.1754}$	$35.243 \pm_{-1.9962}^{+2.0368}$	$0.3691 \pm_{-0.0545}^{+0.0687}$

**Notes.** Column description: Bayesian best-fit slope ( $m$ ) and lower and upper errors (Column 1); intercept ( $c$ ) and lower and upper errors (Column 2); and intrinsic scatter ( $s$ ) and lower and upper errors (Column 3) of the relation  $\log(L_X) = m \times \log(M_{\text{stellar}}) + c + \epsilon$ , where  $\epsilon$  is a random variable with variance equal to  $s^2$ .

applied. In order to best determine the statistical contribution from the MMG, given that we may have missed some of these galaxies, we re-calculate the group stellar mass *excluding* the MMG, and use the difference between this value and that found for the group including all members to characterize the fraction  $M_{\text{stellar}}^{\text{MMG}}/M_{\text{stellar}}$ . For underluminous systems, the median contribution of the MMG to the total group stellar mass ( $M_{\text{stellar}}^{\text{MMG}}/M_{\text{stellar}}$ ) is lower ( $\sim 36\%$ ) than that found for all systems ( $\sim 42\%$ ) with the most underluminous systems having less of their mass contributed from this member.

To test the significance of the difference in the contribution of the MMG to the total stellar mass between underluminous and the total population of groups, we first create a sample matched in group stellar mass to our underluminous groups from the complete sample of X-ray and optical systems. This process is repeated 10,000 times, calculating  $M_{\text{stellar}}^{\text{MMG}}/M_{\text{stellar}}$  for each group in each sample. Finally, we calculate for each sample the number of systems having  $M_{\text{stellar}}^{\text{MMG}}/M_{\text{stellar}} < 40\%$  (above the peak of the underluminous distribution). For the underluminous groups, this is 80% of 15 groups. Only 89 of the 10,000 matched samples meet this criterion—i.e., having  $\geq 80\%$  of groups with  $M_{\text{stellar}}^{\text{MMG}}/M_{\text{stellar}} < 40\%$ —indicating that the difference is indeed significant. This may imply that in the underluminous systems less IGM is available from relatively equal mass progenitors (which leads to the group not having a single dominant galaxy). The existence and possible origins of X-ray underluminous or “dark” systems remains a topic of vigorous debate even in the cluster regime where X-ray and spectroscopic data are abundant. A recent study of the maxBCG clusters and an X-ray bright subsample of the clusters by the Planck Collaboration (2011) finds evidence for a possible X-ray underluminous population which shows a low Sunyaev–Zel’dovich signal normalization, while Andreon & Moretti (2011) find no evidence for a significant population of underluminous systems in a study of X-ray luminosity in color-selected clusters. The Rykoff et al. (2008) comparison of X-ray and optically selected clusters suggests there is a wide

range of  $L_X$  at fixed mass, and that X-ray selection simply picks off the more X-ray luminous part of the population.

The overall fraction of gas scales with halo mass, with clusters having a higher gas mass fraction than groups (e.g., Sun et al. 2009; Pratt et al. 2009; Giodini et al. 2009; Peebles & Shankar 2011). To explore why groups with similar total stellar mass may have lower gas mass and a lower contribution of stellar mass from the most massive member, we contrast two modes of group assembly. In the first scenario, the group begins with a massive galaxy and accretes mass smoothly. In the second, roughly equivalent mass “subgroups” (clumps) comprised of similar mass/luminosity galaxies merge. The former case would result in a group with both a higher gas fraction and a more massive central galaxy. We posit this may be one explanation for the observed correlation between the fraction of mass in the MMG, and the relative X-ray luminosity. Popesso et al. (2007) use an optically selected cluster sample to explore the nature of underluminous systems, finding evidence that these systems are undergoing a phase of mass accretion and are still accreting intracluster gas or in the process of merging. In the future, it would be interesting to examine the galaxy population in our groups to examine the role of the X-ray emitting hot medium in driving galaxy evolution in this mass regime.

Examining the positions of the optically and X-ray-selected overluminous systems on the  $M_{\text{dyn}}-L_X$  relation (bottom panel of Figure 14), indicated by open cyan squares, the dynamical masses of the former are all very high ( $\gtrsim 10^{14} M_{\odot}$ ) while the latter span the entire range in  $M_{\text{dyn}}$ . The median contribution of the MMG to the total group stellar mass ( $M_{\text{stellar}}^{\text{MMG}}/M_{\text{stellar}}$ ) is higher ( $\sim 47\%$ ) for overluminous systems than for all systems ( $\sim 42\%$ ). As for the underluminous groups, we test the significance of this difference in the relative contribution from the MMG by creating a sample matched in mass to our overluminous groups from the complete sample of X-ray and optical systems. In this case, we calculate for each sample the number of systems having  $M_{\text{stellar}}^{\text{MMG}}/M_{\text{stellar}} > 50\%$ . For the overluminous groups, this

is 47% of 17 groups. Eight hundred forty-five of the 10,000 matched samples meet this criterion, having  $\geq 47\%$  of groups with  $M_{\text{stellar}}^{\text{MMG}}/M_{\text{stellar}} > 50\%$ , indicating that this difference is not as significant as that found for underluminous systems.

### 13. CONCLUSIONS

We have defined two group samples at  $0.12 < z < 0.79$  in the same fields, one containing 39 high-quality X-ray-selected systems and the other 38 optically selected systems, in order to study groups spanning a significant mass and evolutionary range. Group membership was defined and we applied three different radial cuts: two  $r_{200}$  cuts (roughly approximating a virial radius) based on the X-ray emission and velocity dispersion of the systems; and a constant 1 Mpc cut. Group masses were estimated from X-ray and dynamical characteristics and stellar content—the latter two within the differing radial cuts. Dynamical complexity and substructure was explored using the AD and DS tests and the shape of X-ray emission. We presented the  $L_X$ - $\sigma$  relation for our systems which is similar to that found for nearby groups and discussed the effects of centering, radial cuts and dynamical complexity/substructure in regards to outliers in this, and other scaling relations. Best fits to this, and to  $L_X$ - $M_{\text{stellar}}$  relations for different group samples and radial cuts were presented. Stellar mass fractions were estimated using the X-ray and dynamical mass as proxies for the group halo mass. Finally, evidence for a population of optical systems seemingly underluminous in X-rays given their stellar and dynamical mass was discussed. Our main conclusions are as follows.

1. *Confusion.* Confusion exists both in matching galaxies to extended X-ray emission and matching X-ray emission to already identified optical systems. Until X-ray spectroscopy is available to measure the redshift of the X-ray emitting gas, completely confident matching will not be possible. Splitting systems into X-ray detected and undetected systems designates the problem, not the solution. These difficulties in matching make cosmological studies using groups difficult.
2. *Dynamical complexity.* Dynamical complexity/substructure in a system *can* work to inflate velocity dispersion and stellar mass and may explain the position of certain outliers in the scaling relations explored here. It is important to recall that the tests we are using are orbit dependent and can only be confidently applied to systems having at least 10 members.
3. *Radial cuts.* Applying X-ray-based  $r_{200}$  radial cuts usually produces the tightest scaling relations. The good correlation between  $L_X$  and  $\sigma$  and the lack of dynamical complexity found for systems using this radius implies that it is isolating the virialized part of the group. Velocity dispersion based and constant cuts generally result in larger radii, more members, and include more substructure/non-Gaussianity. This acts to increase scatter and inflate both velocity dispersion and stellar mass. However, as some systems are not X-ray detected, such cuts are the only options.
4. *Stellar mass fraction.* We find a mean stellar mass fraction of  $\sim 0.014$  within an X-ray-based  $r_{200}$  and treating the X-ray mass as the total mass of the system. This is comparable to those found by Giodini et al. (2009), Balogh et al. (2011a), and Leauthaud et al. (2012) but significantly lower than that found by Gonzalez et al. (2007). The mean contribution of the MMG is  $\sim 0.004$ . Using a total mass based on dynamical mass would result in different fractions due to significant disagreement between  $M_X$  and  $M_{\text{dyn}}$  for many of our systems.
5. *Total mass measures.* The differences in total mass measures ( $M_X$  and  $M_{\text{dyn}}$ ) tend to increase, and the scatter decrease, as X-ray mass increases.
6. *X-ray underluminous groups.* We define a sample of systems as X-ray underluminous given their stellar mass, the majority of which are optically selected. Not all such systems show dynamical complexity and the stellar mass fraction in the MMG of these systems is on average less than that found for the total population of groups. This may indicate that less IGM is being contributed from the progenitor halo containing the most massive member and we posit that differences in accretion (a continuous smooth accretion of galaxies from the field verses the merging of similar mass “subgroups”) may be one explanation for the observed correlation between the fraction of mass in the MMG and the relative X-ray luminosity.

We thank the CNOC2 team for the use of their unpublished data. This research uses observations made with ESO Telescopes at Paranal (program ID 080.A-0427 and 081.A-0103) and the Magellan telescopes operated by The Carnegie Institution of Washington. We acknowledge the use of the FORS and COSMOS pipelines and thank Dr. Carlo Izzo at ESO for pipeline assistance and Renbin Yan for providing the ZSPEC software. We thank Russell Blackport for the reduction of and measurements of redshifts from GMOS data. L.C.P. acknowledges support from an NSERC Discovery grant. J.L.C. thanks Francesco Montesano, Stefania Giodini, Marisa Girardi, and the referee for valuable input.

*Facilities:* VLT:Antu (FORS2), Magellan:Baade (LDSS2 imaging spectrograph), CFHT (WIRCAM), NTT (SOFI), XMM, CXO, GALEX

### REFERENCES

- Andreon, S. 2010, *MNRAS*, 407, 263  
 Andreon, S., & Moretti, A. 2011, *A&A*, 536, A37  
 Appenzeller, I., Fricke, K., Fürtig, W., et al. 1998, *Messenger*, 94, 1  
 Balogh, M. L., Babul, A., Voit, G. M., et al. 2006, *MNRAS*, 366, 624  
 Balogh, M. L., Mazzotta, P., Bower, R. G., et al. 2011a, *MNRAS*, 412, 947  
 Balogh, M. L., McGee, S. L., Wilman, D., et al. 2009, *MNRAS*, 398, 754  
 Balogh, M. L., McGee, S. L., Wilman, D. J., et al. 2011b, *MNRAS*, 412, 2303  
 Balogh, M. L., Wilman, D., Henderson, R. D. E., et al. 2007, *MNRAS*, 374, 1169  
 Beers, T. C., Flynn, K., & Gebhardt, K. 1990, *AJ*, 100, 32  
 Bruzual, G., & Charlot, S. 2003, *MNRAS*, 344, 1000  
 Cappellari, M., Bacon, R., Bureau, M., et al. 2006, *MNRAS*, 366, 1126  
 Carlberg, R. G., Yee, H. K. C., & Ellingson, E. 1997, *ApJ*, 478, 462  
 Carlberg, R. G., Yee, H. K. C., Morris, S. L., et al. 1999, *Phil. Trans. R. Soc. A*, 357, 167  
 Carlberg, R. G., Yee, H. K. C., Morris, S. L., et al. 2001, *ApJ*, 552, 427  
 Chabrier, G. 2003, *ApJ*, 586, L133  
 Charlot, S., & Fall, S. M. 2000, *ApJ*, 539, 718  
 Christensen, N., & Meyer, R. 2000, arXiv:astro-ph/0006401  
 Cooper, M. C., Newman, J. A., Coil, A. L., et al. 2007, *MNRAS*, 376, 1445  
 D’Agostino, R., & Stephens, M. 1986, *Goodness-of-fit Techniques* (New York: Dekker)  
 Davis, M., Faber, S. M., Newman, J., et al. 2003, *Proc. SPIE*, 4834, 161  
 Davis, M., Guhathakurta, P., Konidaris, N. P., et al. 2007, *ApJ*, 660, L1  
 Dressler, A., & Shectman, S. A. 1988, *AJ*, 95, 985  
 Dunkley, J., Komatsu, E., Nolte, M. R., et al. 2009, *ApJS*, 180, 306  
 Efron, B. 1982, *The Jackknife, the Bootstrap, and Other Resampling Plans* (CBMS-NSF Regional Conference Series in Applied Mathematics; Philadelphia: SIAM)  
 Eke, V. R., Baugh, C. M., Cole, S., et al. 2004, *MNRAS*, 348, 866  
 Eke, V. R., Baugh, C. M., Cole, S., et al. 2005, *MNRAS*, 362, 1233

- Finoguenov, A., Connelly, J. L., Parker, L. C., et al. 2009, *ApJ*, 704, 564
- Finoguenov, A., Guzzo, L., Hasinger, G., et al. 2007, *ApJS*, 172, 182
- Gerke, B. F., Newman, J. A., Faber, S. M., et al. 2007, *MNRAS*, 376, 1425
- Gilks, W. R., Richardson, S., & Spiegelhalter, D. J. 1996, *Markov Chain Monte Carlo Methods in Practice* (London: Chapman and Hall)
- Giodini, S., Pierini, D., Finoguenov, A., et al. 2009, *ApJ*, 703, 982
- Girardi, M., Giuricin, G., Mardirossian, F., Mezzetti, M., & Boschin, W. 1998, *ApJ*, 505, 74
- Girardi, M., & Mezzetti, M. 2001, *ApJ*, 548, 79
- Glazebrook, K., & Bland-Hawthorn, J. 2001, *PASP*, 113, 197
- Gonzalez, A. H., Zaritsky, D., & Zabludoff, A. I. 2007, *ApJ*, 666, 147
- Henderson, R. D. E. 2010, Master's thesis, McMaster Univ.
- Horner, D. J. 2001, PhD thesis, Univ. Maryland College Park
- Hou, A., Parker, L. C., Harris, W. E., & Wilman, D. J. 2009, *ApJ*, 702, 1199
- Hou, A., Parker, L. C., Wilman, D. J., et al. 2012, *MNRAS*, 421, 3594
- Iovino, A., Cucciati, O., Scodreggio, M., et al. 2010, *A&A*, 509, A40
- Jeltema, T. E., Mulchaey, J. S., & Lubin, L. M. 2008, *ApJ*, 685, 138
- Jeltema, T. E., Mulchaey, J. S., Lubin, L. M., & Fassnacht, C. D. 2007, *ApJ*, 658, 865
- Kelly, B. C. 2007, *ApJ*, 665, 1489
- Kelson, D. D. 2003, *PASP*, 115, 688
- Kovač, K., Lilly, S. J., Knobel, C., et al. 2010, *ApJ*, 718, 86
- Leauthaud, A., Finoguenov, A., Kneib, J., et al. 2010, *ApJ*, 709, 97
- Leauthaud, A., George, M. R., Behroozi, P. S., et al. 2012, *ApJ*, 746, 95
- Lilly, S. J., Le Brun, V., Maier, C., et al. 2009, *ApJS*, 184, 218
- Łokas, E. L., & Mamon, G. A. 2001, *MNRAS*, 321, 155
- Mahdavi, A., & Geller, M. J. 2001, *ApJ*, 554, L129
- McGee, S. L., Balogh, M. L., Henderson, R. D. E., et al. 2008, *MNRAS*, 387, 1605
- McGee, S. L., Balogh, M. L., Wilman, D. J., et al. 2011, *MNRAS*, 413, 996
- Mulchaey, J. S., Davis, D. S., Mushotzky, R. F., & Burstein, D. 2003, *ApJS*, 145, 39
- Nelson, L. 1998, *J. Qual. Technol.*, 30, 298
- Osmond, J. P. F., & Ponman, T. J. 2004, *MNRAS*, 350, 1511
- Peeples, M. S., & Shankar, F. 2011, *MNRAS*, 417, 2962
- Pinkney, J., Roettiger, K., Burns, J. O., & Bird, C. M. 1996, *ApJS*, 104, 1
- Planck Collaboration, Aghanim, N., Arnaud, M., et al. 2011, *A&A*, 536, A12
- Popesso, P., Biviano, A., Böhringer, H., & Romaniello, M. 2007, *A&A*, 461, 397
- Pratt, G. W., Croston, J. H., Arnaud, M., & Böhringer, H. 2009, *A&A*, 498, 361
- Ramella, M., Boschin, W., Geller, M. J., Mahdavi, A., & Rines, K. 2004, *AJ*, 128, 2022
- Rykoff, E. S., Evrard, A. E., McKay, T. A., et al. 2008, *MNRAS*, 387, L28
- Salim, S., Rich, R. M., Charlot, S., et al. 2007, *ApJS*, 173, 267
- Sanderson, A. J. R., Edge, A. C., & Smith, G. P. 2009, *MNRAS*, 398, 1698
- Serra, A. L., Diaferio, A., Murante, G., & Borgani, S. 2011, *MNRAS*, 412, 800
- Sun, M., Voit, G. M., Donahue, M., et al. 2009, *ApJ*, 693, 1142
- Wilman, D. J., Balogh, M. L., Bower, R. G., et al. 2005a, *MNRAS*, 358, 71
- Wilman, D. J., Balogh, M. L., Bower, R. G., et al. 2005b, *MNRAS*, 358, 88
- Wilman, D. J., Oemler, A., Jr., Mulchaey, J. S., et al. 2009, *ApJ*, 692, 298
- Wilman, D. J., Pierini, D., Tyler, K., et al. 2008, *ApJ*, 680, 1009
- Xue, Y.-J., & Wu, X.-P. 2000, *ApJ*, 538, 65
- Yang, X., Mo, H. J., & van den Bosch, F. C. 2009, *ApJ*, 695, 900
- Yee, H. K. C., Morris, S. L., Lin, H., et al. 2000, *ApJS*, 129, 475
- Zabludoff, A. I., & Mulchaey, J. S. 1998, *ApJ*, 496, 39
- Zabludoff, A. I., & Mulchaey, J. S. 2000, *ApJ*, 539, 136
- Zhang, Y.-Y., Andernach, H., Caretta, C. A., et al. 2011, *A&A*, 526, A105